

THIS FILE CORRECTION

4

MEMORANDUM REPORT BRL-MR-3752

BRL**AD-A208 099**

**PREDICTION AND COMPARISON
WITH MEASUREMENTS OF THE AERODYNAMIC
CHARACTERISTICS OF FLARE-STABILIZED
XM910 PROTOTYPES**

**JAMES E. DANBERG
ASHER SIGAL
ILMARS CELMINS**

MAY 1989

DTIC
ELECTE
MAY 26 1989
S E D

APPROVED FOR PUBLIC RELEASE; DISTRIBUTION UNLIMITED.

U.S. ARMY LABORATORY COMMAND

**BALLISTIC RESEARCH LABORATORY
ABERDEEN PROVING GROUND, MARYLAND**

89 5 25 047

UNCLASSIFIED
SECURITY CLASSIFICATION OF THIS PAGE

SEC-CLASSREPORT DOCUMENTATION PAGE				Form Approved OMB No. 0704-0188	
1a. REPORT SECURITY CLASSIFICATION UNCLASSIFIED			1b. RESTRICTIVE MARKINGS		
2a. SECURITY CLASSIFICATION AUTHORITY			3. DISTRIBUTION/AVAILABILITY OF REPORT Approved for public release, distribution unlimited.		
2b. DECLASSIFICATION/DOWNGRADING SCHEDULE			5. MONITORING ORGANIZATION REPORT NUMBER(S)		
4. PERFORMING ORGANIZATION REPORT NUMBER(S) BRL-MR-3752			7a. NAME OF MONITORING ORGANIZATION		
6a. NAME OF PERFORMING ORGANIZATION US Army Ballistic Research Laboratory		6b. OFFICE SYMBOL (If applicable) SLCBR-LF	7b. ADDRESS (City, State, and ZIP Code)		
6c. ADDRESS (City, State, and ZIP Code) Aberdeen Proving Ground, Maryland 21005-5066			9. PROCUREMENT INSTRUMENT IDENTIFICATION NUMBER		
8a. NAME OF FUNDING/SPONSORING ORGANIZATION		8b. OFFICE SYMBOL (If applicable)	10. SOURCE OF FUNDING NUMBERS		
8c. ADDRESS (City, State, and ZIP Code)			PROGRAM ELEMENT NO. 62618A	PROJECT NO. 11162618AH80	TASK NO. 00
				WORK UNIT ACCESSION NO. 001 A1	
11. TITLE (Include Security Classification) PREDICTION AND COMPARISON WITH MEASUREMENTS OF THE AERODYNAMIC CHARACTERISTICS OF FLARE-STABILIZED XM910 PROTOTYPES					
12. PERSONAL AUTHOR(S) DANBERG JAMES E, SIGAL ASHER* and CEIMINS TIMADS					
13a. TYPE OF REPORT Memorandum Report		13b. TIME COVERED FROM TO		14. DATE OF REPORT (Year, Month, Day)	
15. PAGE COUNT					
16. SUPPLEMENTARY NOTATION *Associate Professor of Aeronautics, Department of Aeronautical Engineering, Technion, Haifa 32000, Israel					
17. COSATI CODES			18. SUBJECT TERMS (Continue on reverse if necessary and identify by block number)		
FIELD	GROUP	SUB-GROUP	Preliminary Projectile Design XM910		
01	01		Multi-Stage Projectile, Aerodynamics of Projectiles,		
19	01		Fast Aerodynamic Prediction, Hypersonic Aerodynamics		
19. ABSTRACT (Continue on reverse if necessary and identify by block number)					
<p>A systematic study of a number of flare-stabilized projectile geometries has been undertaken at the US Army Ballistic Research Laboratory (BRL). Ten projectile configurations having identical forebodies and a variety of flares were tested in the BRL Aerodynamics Ballistic Range and the results compared to numerical computations based on two design codes and a Parabolized Navier-Stokes (PNS) code. The design codes, in general, gave good results. The PNS code complimented these results by providing more details on the development of the aerodynamic forces.</p> <p>The results show the drag and stability trade-offs involved for the different configurations. This information can be used to tailor the flare geometry to meet future mission requirements. <i>Keywords:</i></p>					
20. DISTRIBUTION/AVAILABILITY OF ABSTRACT <input type="checkbox"/> UNCLASSIFIED/UNLIMITED <input type="checkbox"/> SAME AS RPT. <input type="checkbox"/> DTIC USERS			21. ABSTRACT SECURITY CLASSIFICATION UNCLASSIFIED		
22a. NAME OF RESPONSIBLE INDIVIDUAL James E. Danberg			22b. TELEPHONE (Include Area Code) (301) 278-4280		22c. OFFICE SYMBOL SLCBR-LF-C

DD Form 1473, JUN 86

Previous editions are obsolete.

SECURITY CLASSIFICATION OF THIS PAGE

UNCLASSIFIED

TABLE OF CONTENTS

	Page
I. INTRODUCTION	1
1. DESCRIPTION OF THE CONFIGURATIONS	1
2. EXPERIMENT	2
II. DESIGN CODE ANALYSIS	2
1. SELECTION OF A DESIGN CODE	2
2. CHOICE OF DESIGN OPTIONS	3
3. PRESENTATION OF THE NON-CIRCULAR STABILIZERS	4
4. THE DRAG OF THE BUTTRESS GROOVES	5
5. CORRECTION FOR THE TRUNCATED NOSE	5
6. COMMENTS	6
III. PARABOLIZED NAVIER-STOKES CODE	6
1. BASE PRESSURE AND BASE DRAG	7
IV. RESULTS	8
1. DRAG BREAK-DOWN AND MACH NUMBER DEPENDENCE	8
2. SLOPE OF THE NORMAL FORCE AND CENTER OF PRESSURE	9
3. EFFECTS OF AFTERBODY SHAPE ON AERODYNAMICS	9
4. PRESSURE DISTRIBUTIONS	10
5. SKIN FRICTION DISTRIBUTION	11
6. NORMAL FORCE DISTRIBUTION	11
7. EVALUATION OF THE MOST EFFECTIVE CONFIGURATION	12
V. CONCLUSIONS	12
VI. RECOMMENDATIONS	12
REFERENCES	37
LIST OF SYMBOLS	39
DISTRIBUTION LIST	41

LIST OF FIGURES

Figure		Page
1	Sketch of baseline projectile with CS-V4-1 flare afterbody.	15
2	Afterbody and extension configurations.	15
3	Spark shadowgraph of CS-V4-1 baseline projectile in flight (low yaw). . . .	16
4	Spark shadowgraph of CS-V4-1 baseline projectile in flight (high yaw). . .	16
5	Comparison between predicted characteristics of a cone-cylinder body and Barth's data for the slope of normal-force curve.	17
6	Comparison between predicted characteristics of a cone-cylinder body and Barth's data for the center-of-pressure location.	17
7	Comparison between computed forebody characteristics for the slope of normal-force curve.	18
8	Comparison between computed forebody characteristics and empirical data for the location of center-of-pressure.	18
9	Geometry of equivalent flare stabilizers.	19
10	Axial-force coefficient as a function of Mach number for the CS-V1 configuration.	20
11	Axial-force coefficient as a function of Mach number with component brake-down for the CS-V2 configuration.	21
12	Comparison between analysis and range results for the slope of the normal-force curve as a function of Mach number.	22
13	Comparison between analysis and range results for the location of the center-of-pressure as a function of Mach number.	23
14	Zero lift drag coefficient for all configurations at $M_\infty=4.0$	24
15	Slope of the pitching moment coefficient about the center of gravity at $M_\infty=4.0$	25
16	Slope of the lift coefficient for all configurations at $M_\infty=4.0$	26
17	Center of pressure location from the projectile nose for all configurations at $M_\infty=4.0$	27
18	Wall pressure distribution for configuration CS-V2 at three Mach numbers.	28
19	Wall pressure distribution for five configurations at $M_\infty=4.0$, $\alpha = 1^\circ$, lee-side.	29
20	Skin friction coefficient distribution for configuration CS-V2 at three Mach numbers.	30

21	Skin friction coefficient distribution for five configurations at $M_\infty=4.0$, $\alpha = 0^\circ$	31
22	Normal-force distribution for six configurations at $M_\infty=4.0$ $\alpha = 0^\circ$	32
23	Comparison between Second Order Shock Expansion and PNS normal-force distribution.	33
24	Comparison between Second Order Shock Expansion and PNS circumferential pressure distribution on the flare.	34
25	Correlation of drag coefficient with center of pressure location at $M_\infty=4.0$	35

LIST OF TABLES

Table		Page
1	GEOMETRICAL PARAMETERS OF THE XM910 CS-FAMILY OF PROJECTILES	2
2	TYPICAL TABULATED XM910 RESULTS	14

Accession For	
NTIS	<input checked="" type="checkbox"/>
DTIC TAB	<input type="checkbox"/>
Unannounced	<input type="checkbox"/>
Justification	
By	
Distribution/	
Availability Codes	
Avail and/or	
Dist	Special
A-1	



I. INTRODUCTION

Flare-stabilized projectiles are currently being evaluated for a variety of applications, including a 25 mm training round.¹ A systematic study of a number of flare geometries has been undertaken at the U.S. Army Ballistic Research Laboratory. The ultimate objectives of the study are: 1.) to determine how to increase the stability of a flare-stabilized round with a minimum increase in drag; and 2.) to provide a range of aerodynamic data with which to determine the capabilities and limitations of available numerical predictive techniques.

1. DESCRIPTION OF THE CONFIGURATIONS

Ten projectile configurations are considered in this investigation, all with basically the same slightly blunted cone-cylinder forebody of almost 12 calibers. The projectile afterbody consists of a stabilizing flare, the angle and length of which were varied to provide a range of flare shapes. Figure 1 shows the overall geometry of the projectile with one of the flares (CS-V4-1) attached.

Figure 2 shows all of the flare geometries. The CS-V1 configuration is a simple 15.2 degree half-angle, 2.67 caliber long flare. The CS-V2 design has a 4 degree, 4.5 caliber flare. The CS-V4 family of flares are all basically derived from a 6 degree, 3.5 caliber baseline flare configuration. Configuration CS-V4-1 is the baseline flare. Configurations CS-V4-2 through CS-V4-5 consist of the baseline flare with one caliber extensions of 6, 0, 12, and -6 degrees, respectively.

Additionally, there are three other configurations in the CS-V4 group that are not simple conic or biconic shapes. CS-V4-7 has a -6 degree boattail, similar to CS-V4-5, but it also has a set of four fins with a 12 degree sweep angle located on the boattail. Configuration CS-V4-8 consists of the baseline configuration with four strakes extending along the length of the flare.

Finally, configuration CS-V4-6 has a non-conical square base. The geometry of this shape was chosen so that the base area would be identical to that of the CS-V4 baseline, and so that the last caliber of length would have a square cross section. This dictates a flare angle of 9.53 degrees.

Note that the basic shape corresponds to that of anti-armor projectiles of relatively large length to diameter ratio (about 16.3) where the center of gravity is near the mid-length. In order to maintain the same weight distribution, the projectile bodies were made of steel and the afterbodies were made of aluminum with an open cavity in the base.

The designations of the ten flares and flare-fin stabilizers and their major geometrical relationships are given in Table 1.

2. EXPERIMENT

A series of test firings have been carried out in the BRL Aerodynamics Range.² Up to four rounds of the CS-V1 and -V2 projectiles were fired at a number of fixed conditions from transonic to 4.6 in Mach number. Four rounds of each of the other flare configurations were fired at a nominal Mach number of 4.0. The sabots used to launch the projectiles incorporated a slip band obturator, which is designed to keep the roll rate at approximately one turn in four meters of travel. Orthogonal spark shadowgraph pictures (see Figures 3 and 4 for typical pictures) at stations along the range are interpreted to provide position and orientation throughout the flight. These data are fitted to the linearized equations of motion.³ The fitting provides the linearized aerodynamic coefficient of drag and the slopes of the coefficient of moment and lift versus angle of attack. From the lift, the center-of-pressure is also determined.

TABLE 1: GEOMETRICAL PARAMETERS OF THE XM910 CS-FAMILY OF PROJECTILES

CONFIGURATION	FLARE FINENESS RATIO	FLARE ANGLES	BASE DIAMETER RATIO	MAX. SPAN RATIO	EXTENSION ONE CALIBER
CS-V1	2.67	15.20	2.450		None
CS-V2	4.50	4.00	1.628		None
CS-V4-1	3.50	6.00	1.736		None
CS-V4-2	4.50	6.00	1.948		6.0° Flare
CS-V4-3	4.50	6.00	1.736		Cyl. Skirt
CS-V4-4	4.50	6.00	2.160		12° Biconic
CS-V4-5	4.50	6.00	1.526		-6° Boattail
CS-V4-6	4.50	9.53	1.540		Square Base
CS-V4-7	4.50	6.00	1.226	2.160	Boattail w/ Fins
CS-V4-8	3.50	6.00	1.736	2.043	None

II. DESIGN CODE ANALYSIS

Two kinds of predictive techniques have been applied to the family of configurations: fast turnaround design codes which are ideally suited to parametric studies; and the Parabolized Navier-Stokes (PNS) technique for solving the supersonic, thin shear layer equations of motion.

1. SELECTION OF A DESIGN CODE

The Missile DATCOM⁴ and the NSWC Aeroprediction⁵ codes are capable of analyzing the aerodynamic characteristics of the proposed XM910 configurations. The two codes use

the same two methods for the evaluation of the inviscid contribution to the aerodynamic coefficients at supersonic speeds. They are Van Dyke's hybrid method⁶ and Syvertson and Dennis Second Order Shock Expansion (SOSE) method.⁷ Indeed, both codes yield practically the same results for the normal-force and pitching-moment coefficients at small angles-of-attack and the same zero lift wave drag coefficients.

In the transonic region, the codes use data bases for the evaluation of the normal-force and the pitching moment coefficients. The accuracy of the two data bases was evaluated by comparing predictions by the two codes with the experimental data of Barth.⁸ The configuration selected for the comparison is a cone-cylinder having component fineness ratios of 2.5 and 6.0, respectively. This configuration is similar to that of the forebody of the subject round.

The results of the comparison are shown in Figures 5 and 6. The slope of the normal-force curve predicted by the DATCOM code is in excellent agreement with the experimental data base. The NSWC code predicts a slope which is 11 to 27 per cent lower than the experimental values. The DATCOM code predicts the location of the center-of-pressure within 0.25 diameters and better than the NSWC code. These findings concerning the data base of the NSWC code are consistent with previous conclusions of Sigal.⁹ It was decided to use the DATCOM code for the evaluation of the aerodynamic coefficients in the pitch plane.

The two codes use different empirical methodologies for the estimation of the viscous contributions to the axial force coefficient. Since the outputs are different, these contributions were compared with the empirical data reported by Stoney.¹⁰ It was found that the DATCOM code over-predicts the base drag coefficient of bodies having flares. The NSWC-Aeroprediction code provides reliable prediction of the base drag coefficient for cylindrical and flared bodies. It uses an empirical data base for the estimation of the skin-friction coefficient in a wide range of Reynolds numbers, including the region of transition. This capability is of importance in the present case since the small projectile flies, most of the time, in the transition zone. The NSWC code was selected for the evaluation of the axial-force coefficient.

2. CHOICE OF DESIGN OPTIONS

In the beginning, the two options for calculations at supersonic speeds were tried, in an attempt to find the best cross-over Mach number between the Van Dyke and the SOSE methods. However, when the results were analyzed, it was found that the Van Dyke method failed in the case of bodies with flares. The computed pressure distribution along the flare showed a dip, followed by a rise. This distribution is physically unreasonable. Hence, only the SOSE method was used. Since this method is valid mainly for high Mach numbers, it is desirable to evaluate its accuracy at the low end of the supersonic region. This was done by comparing analytical results for an extended nose forebody with empirical data bases. The British Engineering Science Data Units (ESDU),¹¹ Aircraft DATCOM,¹² and AMICOM,¹³ data bases were used and the results are shown in Figures 7 and 8. The first figure shows that the SOSE method is in very good agreement in normal-force curve slope at Mach numbers larger than 3.0 with the ESDU and Aircraft DATCOM data. In the lower

range, the method over-predicts the empirical data by about 20 per cent. The center-of-pressure location is well predicted by the SOSE method. Note that since the AMICOM data is only available for the nose fineness ratio of 4.0, it was adjusted by multiplying the center-of-pressure distance, measured from the tip, by the ratio of nose fineness ratios.

An attempt to use the truncated nose option in the code yielded a very large reduction in normal-force curve slope, accompanied by a forward shift in the center-of-pressure. These changes are a result of the code accounting for losses through a normal shock wave and not considering the mixing in the entropy layer. It was decided to extend the nose, in the computational model, to form a complete cone and to apply corrections for the effect of bluntness, based on empirical data, that will be described in section 5.

3. PRESENTATION OF THE NON-CIRCULAR STABILIZERS

Three configurations feature non-circular stabilizers. Configuration CS-V4-3 has a square base and CS-V4-7 and -8 have lifting surfaces mounted on the flares. Neither feature can be handled by the design codes presently available at the Launch and Flight Division. Hence, equivalent axisymmetric configurations were used as computational models in these cases. Their cross-sectional area distribution provide the same normal-force curve slope distribution as that of the actual configurations, evaluated by slender body theory.

Using center body cross sectional area as reference area for the equivalent body, the above condition becomes:

$$\left(\frac{S C_{N_a}}{S_R}\right)_e = \frac{S C_{N_a}}{S_R} \quad (1)$$

Since the equivalent body is circular

$$\left(\frac{S C_{N_a}}{S_R}\right)_e = 2\left(\frac{d}{D}\right)^2 \quad (2)$$

For a slender body having a square cross-section, of dimension d on a side, Nielsen,¹⁴ gives:

$$\frac{S C_{N_a}}{S_R} = \frac{2.4d^2}{S_R} = 3.056\left(\frac{d}{D}\right)^2 \quad (3)$$

Hence, for a square afterbody

$$\frac{D_e}{D} = 1.236 \frac{d}{D} \quad (4)$$

For a cruciform slender wing-body combination the same reference gives

$$\frac{S C_{N_a}}{S_R} = 2\left(\frac{b}{D}\right)^2 \left[1 - \left(\frac{D_b}{b}\right)^2 + \left(\frac{D_b}{b}\right)^4\right] \quad (5)$$

so that

$$\frac{D_e}{D} = \frac{b}{D} \left[1 - \left(\frac{D_b}{b}\right)^2 + \left(\frac{D_b}{b}\right)^4\right]^{\frac{1}{2}} \quad (6)$$

The main geometrical parameters for the equivalent afterbodies are:

CONFIGURATION	D_e/D	
	$x/d=15.65$	$X/D=16.65$
CS-V4-6	1.900	1.900
CS-V4-7	1.736	1.870
CS-V4-8	1.826	—

A graphical comparison between the equivalent and the actual afterbodies is shown in Figure 9.

4. THE DRAG OF THE BUTTRESS GROOVES

This contribution to the axial-force coefficient is not included in the design codes. It is evaluated using the method of equivalent sand roughness and a new correlation for two dimensional, ridge-type, roughness elements, compiled by Sigal.¹⁵ The ratio of the equivalent sand roughness to the height of the buttress grooves is estimated to be 2.0. The amplification in the skin-friction due to the roughness is evaluated using a friction law also compiled in Reference 15. The additional drag coefficient, due to the grooves, is related to the amplified skin friction by:

$$\Delta C_{D_{BT}} = \frac{A_{bg}}{S_R} \left(\frac{C_f}{C_{fo}} - 1 \right) C_{fo} \quad (7)$$

The dependence of this contribution upon Mach number depends on the wall temperature conditions. A cold wall case is assumed here, where the wall temperature equals the free-stream temperature because it approximately represents the conditions in the aerodynamic range tests, where the time of flight is too short for pronounced aerodynamic heating. In the transonic region the difference between a cold and adiabatic wall conditions is small. As Mach number increases the adiabatic wall case yield a smaller contribution, due to the increase in wall temperature.

5. CORRECTION FOR THE TRUNCATED NOSE

As discussed above, the nose in the computational model was extended to form a complete cone. The correction due to the actual geometry is based on empirical data.

The systematic data base of Owens,¹⁶ for spherically blunted cones, is used for the correction of the normal-force and the center-of-pressure location. Results for a half cone angle of 10 degrees are used because they are closest to the present geometry. The effects of bluntness is a slight decrease in normal-force curve slope and a very slight forward shift in the center-of-pressure.

Since no data were found for truncated cones, the estimate of the effect of truncation on the axial-force coefficient is based on the data of Esch¹⁷ for truncated ogives.

The equivalent configuration used for the evaluation of the contribution of the skin-friction and the base to the drag coefficient have the same wetted area and base area, as the actual ones.

In the transonic region, the design codes use slender body theory for the evaluation of the contribution of afterbodies to stability. Thus, only base diameter ratio (not the base area distribution) determine the contribution of the stabilizer to the normal-force curve slope. As a result, the design codes yield the same normal-force curve slope and almost the same center-of-pressure location for configurations CS-V4-1 and -3, in the transonic region.

6. COMMENTS

Configuration CS-V4-5 has a boattail mounted on a flare. The flow deflection between these two components is 12 degrees. It is expected that this large deflection will cause separation at transonic and low supersonic Mach numbers. Hence, it is expected that the boattail will be aerodynamically ineffective in these regions and that the aerodynamic characteristics of this configuration will be close to those of CS-V4-1.

The fin of configuration CS-V4-7 is mounted on a boattail identical to that of CS-V4-5. By the same argument, it is expected that the fin will be immersed in separated flow. This will reduce its efficiency as a stabilizer so the aerodynamic characteristics, at transonic speeds, will be close to those of CS-V4-1.

III. PARABOLIZED NAVIER-STOKES CODE

The flow over these configurations also have been computed using the Parabolized Navier-Stokes technique based on the code developed by Schiff and Steger.¹⁸ This technique consists of generalized body fitted coordinates, thin shear layer, linearized, approximately factored equations. A finite difference algorithm is solved implicitly using a block diagonal method as formulated by Beam and Warming.¹⁹ The approximation, which permits marching in the primary flow direction, limits the application to attached, supersonic free-stream flows. Thus, the results from the PNS code cannot provide information on the separated flow in the near wake or the base pressure.

The code uses the Baldwin-Lomax²¹ algebraic turbulence model to compute skin friction forces. The flow is assumed to be turbulent from the nose although this may somewhat overestimate the actual viscous contribution. A new technique,¹⁵ for computing buttress thread and groove effects was applied to this configuration. However, the body is so small (8.28 mm) and the flight Reynolds number is so high that the technique is not valid since the estimated equivalent roughness height is larger than the undisturbed boundary layer thickness. Thus, the same estimate of buttress groove drag which was used for the design codes was also applied to the PNS results.

In principle, the PNS code can handle all the non-conical shapes considered, including the fin and strake bodies but these shapes have not been attempted here. PNS results are reported only for the axisymmetric shapes and the square base configuration. The tabulated PNS results for the wave and friction drag at four Mach numbers are given in Table 2.

Some instability was observed in the PNS calculations at the cylinder-flare junction, particularly for the low Mach numbers. This problem was so severe for the CS-V1 configuration with the 15.2 degree flare that the results were considered unreliable and are not included here. The oscillations for the small flare angles was reduced or eliminated by adding a small fairing between the cylinder and the flare. In all the results cited here, a 0.25 caliber sine function fairing was used to provide a continuous body radius and its first derivative in the transition region. Computations at Mach number 4.0 showed that no fairing was required.

1. BASE PRESSURE AND BASE DRAG

Estimates of the base drag for these projectiles were obtained from the NSWC code which calculates the base pressure from empirical formulas which depend on the equivalent body effective flare angle. In the present case there is some uncertainty in the application to the two element afterbodies of the CS-V4 family of projectiles. An attempt was made to investigate this question by using the results from the more elaborate but still semi-empirical work of Mueller, et al.²⁰ The accuracy of Mueller's method for flared afterbodies has not been generally established; thus, simple correlation formulas have been developed to follow the trend of his results and, as a consequence, these predictions should only be considered as primarily illustrating trends.

The plotted results of Reference 20 suggest that the base pressure can be described by the addition of two terms. The first term represents the base pressure of a long (nose effects neglected), cylindrical afterbody which is primarily a function of Mach number. A simple power law representation for this term is:

$$\left(\frac{p_b}{p_\infty}\right)_{cylinder} = 1.9M_\infty^{-1.46} \quad (8)$$

This expression agrees with experimental data in the Mach number range from 3.0 to 4.0 but predicts too high a base pressure at Mach number of 2.0.

The second term accounts for the angle of the flare, ϕ_f and the length of the afterbody, (L_f/D) . An exponential expression is fitted to Mueller's results. The exponential form is chosen so that near ϕ_f and L_f of zero, the approximation is linear and at larger values of these variables, negative pressures are avoided (although these formulas are only approximately valid for small flare angles less than, 15 degrees, and for Mach numbers in the range from 2.0 to 4.0). The additive effect of flares is :

$$\Delta\left(\frac{p_b}{p_\infty}\right) = -[1 - e^{-0.01\phi_f}][1 - e^{-2.2\frac{L_f}{D}}] \quad (9)$$

Note that ϕ_f is in degrees in this formula.

For the 3.5 and 4.5 caliber flares, the flare length term is essentially unity. Positive ϕ_f 's correspond to flares which reduce the base pressure below that of a cylindrical body. Negative ϕ_f 's, on the other hand are associated with boattails which have increased base pressures.

Most of the CS-V4 series have two element afterbodies consisting of 3.5 caliber, 6

degree flares, followed by one caliber extensions. The above analysis was applied assuming superposition of the flare and extension to the basic cylindrical base pressure. However, there is no theoretical or experimental evidence to justify this procedure. The base pressure is estimated as:

$$\frac{p_b}{p_\infty} = \left(\frac{p_b}{p_\infty}\right)_{cyl} + \Delta\left(\frac{p_b}{p_\infty}\right)_{6^\circ flare} + \Delta\left(\frac{p_b}{p_\infty}\right)_{extension} \quad (10)$$

where equation 9 is used to evaluate both the 6 degree flare and the extension contribution. In the case of the extension, the local body angle was measured relative to the underlying 6 degree flare. The flare length term is essentially unity for the 6 degree flare but does have some effect on the extension contribution.

Table 2 tabulates representative results based on the PNS computation of the wave and friction drag. The base drag coefficient is computed based on the above described formulas, assuming a uniform base pressure acting on the physical base area.

IV. RESULTS

The design codes (NSWC and DATCOM) and the PNS codes have been applied to the configurations of the XM910 prototypes and the main results will be described in terms of the drag, C_{D_o} , slope of the normal force relative to the angle of attack, C_{N_α} , and center of pressure, X_{CP} . This will be followed by some results on the detailed pressure and skin friction distributions.

1. DRAG BREAK-DOWN AND MACH NUMBER DEPENDENCE

Figure 10 shows the variation of the zero yaw drag of the CS-V1 as a function of Mach number. The experimental data are in good agreement with the NSWC codes prediction at supersonic speeds but the code underpredicts the drag at Mach numbers near and below one. It was not possible to reliably calculate this configuration with the PNS code because the 15.2 degree flare caused large oscillations in the calculations. These oscillations are believed to be related to local flow separation. The sharp jump in the predicted drag at transonic speeds ($1.15 < M_\infty < 1.20$) is apparently caused by the switching from the low speed, data base, method of computing drag to the Second Order Shock Expansion (SOSE) method.

Figure 11 shows the Mach number behavior of the smallest flare angle configuration (CS-V2) as well as the components of the drag. Both the modified design code and the PNS code predict the data within the scatter in the measurements above Mach 3. Below that point the scatter in the data becomes large but with the NSWC again underpredicting the data. The base drag, at speeds below about Mach 2., is equal or greater than all the other contributors. The other factors remain surprisingly constant over the Mach number range considered here. The PNS code results are also indicated on the figure. The PNS code can only compute the pressure and friction components of the drag. The base drag has been obtained from the correlations based on Mueller's technique. These calculations have been added to the PNS results as well as the buttress groove drag. These composite

PNS results are in better agreement with the data than those of the design code. However, this is in part due to a higher skin friction drag predicted by the Navier-Stokes code. One reason for the larger friction drag is that turbulent flow was assumed from the start of the numerical computation whereas the design code incorporated an empirical transition and, for this small shell, this makes a significant difference.

2. SLOPE OF THE NORMAL FORCE AND CENTER OF PRESSURE

Figure 12 shows the Mach number dependence of the normal force. The experiments indicate, and both computational methods predict, that there is very little variation of the lift with supersonic Mach number. For the CS-V2 case, both the PNS and DATCOM codes predict the data with equal accuracy. The tendency for the CS-V1 experimental C_{N_α} to increase, above $M_\infty=4.0$, may not be valid because of the large scatter in those particular measurements.

The center of pressure results are given in Figure 13. It is seen that for the CS-V1 case the DATCOM code does well except for a small overprediction at subsonic speeds. However, both codes tend to predict a more forward X_{CP} (by 0.5 to 1.0 caliber) for the 4 degree flare case compared to the data. Thus the lift produced by the flare is higher than estimated by these codes.

3. EFFECTS OF AFTERBODY SHAPE ON AERODYNAMICS

The basic results of this project are contained in Figures 14 through 17. These Figures show the experimental data for drag coefficient, slope of the lift and moment coefficient and the center-of-pressure location obtained from the range tests. The Figures also show the computed results from the design codes and from the PNS code.

Figure 14 shows the zero-lift drag coefficient for all eight configurations at a Mach number of 4.0 and a Reynolds number based on model cylinder diameter of 2.36×10^6 . The baseline configuration, (-1), has a measured drag coefficient of 0.56. The lowest drag is obtained from the boattailed configuration, (-5). This is not surprising since the boattail affects the base pressure, which in turn determines the major component of the drag. The largest drag is produced, as expected, by the biconic shape with its 12 degree flare and consequent high wave drag component.

The prediction techniques determines the drag coefficients quite well. The most probable error between the NSWC Aeroprediction code and the data is 0.027 in drag coefficient. The corresponding value for the PNS results is 0.029.

Figure 15 shows the effect of the different configurations on the pitching moment about the center of gravity of the projectiles. The center of gravity varied only slightly between configurations; the differences in moment are mainly, but not entirely, due to aerodynamic effects. Obviously, the two most stable configurations, (-2) and (-4), are also the configurations with the highest drag. Configuration (-6) has somewhat higher drag than the baseline, but it has much improved stability.

The predictive methods generally give a smaller negative pitching moment. The Second Order Shock Expansion method consistently gives slightly better agreement with the experimental data than the PNS computation.

Figure 16 shows the lift coefficient slope and Figure 17 shows the center-of-pressure measured from the blunted nose of the projectiles. These two figures provide an alternative way of looking at the pitching moment slope results. In general, the Missile DATCOM code adequately predicts both the lift slope and the center-of-pressure, whereas the PNS code consistently underpredicts lift and center-of-pressure. It is possible that the DATCOM results are fortuitous, however, because the DATCOM code predicts the forces neglecting viscous effects. The smooth body viscous effects are accounted for in the PNS code and the afterbody lift is significantly less than predicted by the design code, resulting in the more forward center-of-pressure. However, the buttress grooves are not accounted for in the computations. One possible explanation is that the enlarged boundary layer produced by the grooves is greatly distorted circumferentially at angle of attack so that the lee-side flare becomes less effective relative to the wind-side. An alternate explanation for the lower afterbody lift in the computations, relative to the experiment, is that the cavity in the rear of the models is so large (over 4.0 calibers) that a small internal pressure difference between the top and bottom surfaces could produce a considerable lift with a sufficiently large moment arm to account for the observed discrepancies. CFD studies and solid base experiments are under way to investigate these possibilities.

Although the DATCOM code matches the data fairly accurately, there are some discrepancies between predicted and observed data trends. As can be seen in Figure 15, both the range data and the PNS code show the configuration CS-V4-5 (boattail) is less stable than configuration CS-V4-1 (baseline). The DATCOM results show CS-V4-5 to be more stable. This trend also exists for the lift coefficient slope and center-of-pressure location, although it is not as clearly visible. This reversal of the data trends can lead to serious problems when choosing a projectile geometry for a particular application, which is one function of a projectile design code.

4. PRESSURE DISTRIBUTIONS

One of the primary advantages of using the PNS code is the detail which can be obtained concerning the pressure and force distribution for the various shapes, from which, the overall results of the experiment can be better assessed. Figure 18 shows the wall static pressure for the CS-V2 configuration at three Mach numbers, 2.0, 3.0, and 4.0. The pressures on the conical nose are in very good agreement with cone flow calculations. The pressures on the flares are also approaching cone flow. At the cylinder-flare junction the pressures over-shoot corresponding to local two-dimensional flow conditions. This over-shoot is not abrupt because of the fairing used to prevent oscillations in the PNS code. Figure 19 shows the pressure distribution on the leeward side of the first six configurations at one degree angle of attack. Among the first five configurations, the effectiveness of decreasing the slope of the body on the last caliber is clearly evident. Configuration (-6) produces its higher stabilizing lift because of the larger flare angle (9.53° compared to the 6 degrees of the others) and because of the transition to a square cross section the pressure

drops to nearly the same level as the cylindrical skirt body.

5. SKIN FRICTION DISTRIBUTION

The skin friction distribution for the CS-V2 configuration at three Mach numbers is shown in Figure 20. At a Mach number of 2.0 there is a strong dip at the cylinder-flare junction, despite the 0.25 caliber fairing at that point. This problem almost disappears at the higher Mach numbers. The flare angle of four degrees is so slight that there is only a small increase in friction on the aft flare. There is a strong Mach number effect on the zero pressure gradient boundary layer on the cylinder and the flare which produces a decreasing skin friction drag with increasing Mach number.

Figure 21 shows the effect of five flare configurations on the skin friction distribution. This Figure is for Mach number of 4.0 and zero angle of attack. The PNS code predicts the same skin friction on these five bodies except on the flare extension. The 6 degree flare results in twice the increase in friction as that obtained on the 4 degree flare of the CS-V2 case. The 12 degree biconic flare has the greatest friction increase whereas the friction on the boattail extension drops below the cylinder friction.

6. NORMAL FORCE DISTRIBUTION

Figure 22 shows the distribution of the normal force in terms of the slope of the normal force as a function of X/D for the five configurations. The nose is found to contribute 1.97 to the slope which is 97 per cent of the slender body prediction. The cylindrical mid body contributes only about half of that of the nose at this Mach number but tends to provide an increasing contribution with Mach number. The 8.5 caliber cylinder is sufficiently long so that increasing its length would not provide significant additional lift. The 6 degree, 3.5 caliber flare contributes more lift than the entire forebody. The 12° biconic substantially increases the normal force and stabilizing moment but at the cost of an increase in drag. The boattailed extension (-5) produces only a little less added lift than the cylindrical extension (-3) but with an important decrease in base drag.

Figure 23 shows a comparison between the normal force predicted by the Shock Expansion method, used in the DATCOM and NSWC codes, and the PNS code. It shows that the consistently higher prediction by the SOSE method is because it predicts more lift on the flare. That method is an inviscid one whereas the PNS result takes the viscous flow into account with a reduced efficiency of the flare (85 per cent less normal force for the 4.5 caliber, 6 degree flare). This is further confirmed in comparing the circumferential pressure distribution as shown in Figure 24. The pressure distributions are for a point half the flare length and the predicted pressures levels are significantly different. By subtracting the pressure coefficients at 90°, the difference in the windward and leeward sides which determines the normal force, is displayed. Although the SOSE method gives a larger difference, the distributions are similar.

7. EVALUATION OF THE MOST EFFECTIVE CONFIGURATION

Figure 25 presents the measured data as a correlation of drag coefficient with center of pressure location. This format is chosen to emphasize the trade offs between stability and drag. The "best" configurations have the most rearward center of pressure and the least drag, and are thus located toward the bottom right corner of the figure. A single continuous curve can be drawn through the data of configurations (-1) and (-2) showing the effect of flare length for a single flare angle, i.e., increasing the flare length from 3.5 calibers (configuration (-1)) to 4.5 calibers (configuration (-2)) increases the drag coefficient by 0.12 and shifts the center of pressure back by 1.1 calibers. Configurations (-5), (-3), (-2) and (-4) also form a related series of afterbody shapes, starting with the boattail and ending with the 12 degree biconic body. A curve drawn through these four points shows the effect of the angle of a one caliber extension to the baseline flare. The figure shows that flare extensions with larger angles than the baseline flare are less efficient than simply extending the flare. Conversely, extensions with a shallower flare angle are desirable. The fin configuration (-7), is judged the most effective and (-6) and (-8) are the next most efficient shapes for improving stability at a minimum penalty in drag.

V. CONCLUSIONS

Ten flare-stabilized projectile configurations have been tested in the BRL Aerodynamics Ballistic Range and the results compared to numerical computations based on two design codes and a Parabolized Navier-Stokes code. The evaluation of the results show:

The configuration with a combination of 6 degree flare-boattail with small fins produced the most stable shape with the least drag penalty as compared to conventional flares.

The prediction of the aerodynamic characteristics using the NSWC Aeroprediction code gave, in general, very good results, despite the fact that effective bodies had to be devised to represent the actual body shapes, and that corrections had to be introduced to account for the buttress thread roughness effects. However, some of the data trends for biconic configurations were not predicted correctly.

The Parabolized Navier-Stokes results complemented the semi-empirical computations by providing more detail on the development of the aerodynamic forces. The PNS pitching moment prediction is consistently less than the measurements, possibly because of the effect of the open base cavities or of the buttress groove boundary layer on the projectiles tested.

VI. RECOMMENDATIONS

1. It is recommended not to use the Missile DATCOM code for the evaluation of the axial-force coefficient of bodies with flares, since it over-predicts the contribution of the base.

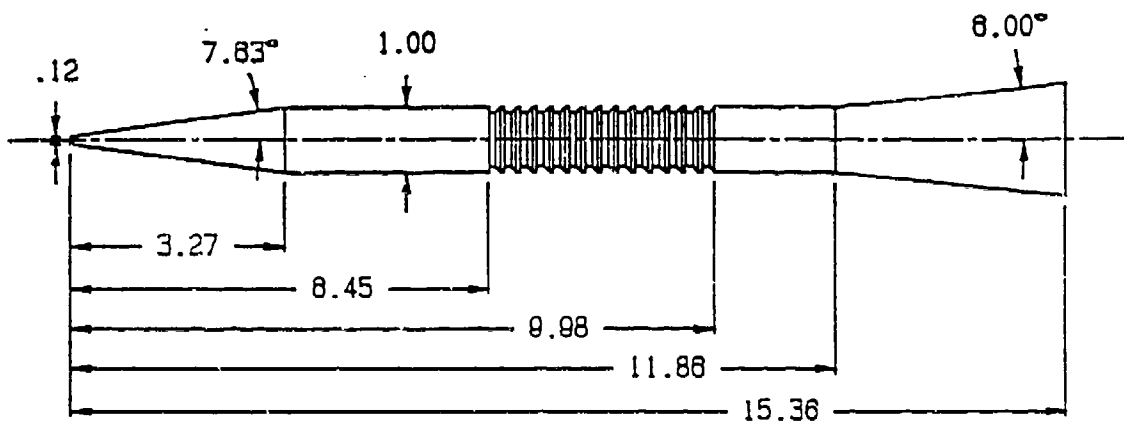
2. It is recommended to use the Missile DATCOM code for predicting the normal-force and the pitching-moment coefficients of bodies in the transonic regime. The reason being the accuracy of its aerodynamic characteristics data base in this Mach number range.

3. It is recommended to use the option of truncated nose, in the DATCOM and NSWC codes, only for configurations having non-small ratio of truncation diameter to maximum diameter. Cases having a slightly truncated nose should be analyzed as if the nose is extended to a point.

4. It is not recommended to use the NSWC or DATCOM codes for design optimization of biconic flared projectiles. These codes do not correctly predict the stabilizing/destabilizing effect of the second flare section.

TABLE 2: TYPICAL TABULATED XM910 RESULTS

MACH NUMBER=2.0							
	C_{D_p}	C_{D_f}	C_{D_b}	$C_{D_{bg}}$	C_D	C_{N_g}	X_{CP}/D
CS-V2	0.150	0.191	0.414	0.090	0.835	5.58	9.26
CS-V4-1	0.227	0.180	0.395	0.090	0.892	5.95	9.29
CS-V4-2	0.270	0.201	0.496	0.090	1.057	7.52	10.43
CS-V4-3	0.224	0.200	0.336	0.090	0.850	6.70	10.07
CS-V4-4	0.528	0.202	0.698	0.090	1.518	8.56	11.45
CS-V4-5	0.303	0.197	0.211	0.090	0.801	6.11	9.47
MACH NUMBER=3.0							
CS-V2	0.122	0.171	0.273	0.080	0.646	5.75	7.76
CS-V4-1	0.180	0.163	0.323	0.080	0.746	5.76	8.64
CS-V4-2	0.214	0.182	0.406	0.080	0.882	7.15	10.12
CS-V4-3	0.178	0.178	0.297	0.080	0.733	6.22	9.20
CS-V4-4	0.408	0.186	0.539	0.080	1.213	8.49	11.12
CS-V4-5	0.217	0.175	0.208	0.080	0.680	5.70	8.52
CS-V4-6				0.080		7.98	10.39
MACH NUMBER=4							
CS-V2	0.105	0.155	0.187	0.060	0.507	5.47	8.13
CS-V4-1	0.155	0.148	0.217	0.060	0.580	5.79	8.33
CS-V4-2	0.186	0.167	0.273	0.060	0.686	7.03	9.73
CS-V4-3	0.154	0.162	0.202	0.060	0.578	6.08	8.70
CS-V4-4	0.348	0.174	0.358	0.060	0.940	8.68	11.01
CS-V4-5	0.177	0.153	0.144	0.060	0.539	5.63	8.17
CS-V4-6				0.060		7.43	9.71
MACH NUMBER=4.6							
CS-V2	0.100	0.110	0.150	0.050	0.410	5.94	7.94



ALL DIMENSIONS IN CALIBERS (1 CALIBER = 8.28 mm)

Figure 1. Sketch of baseline projectile with CS-V4-1 flare afterbody.

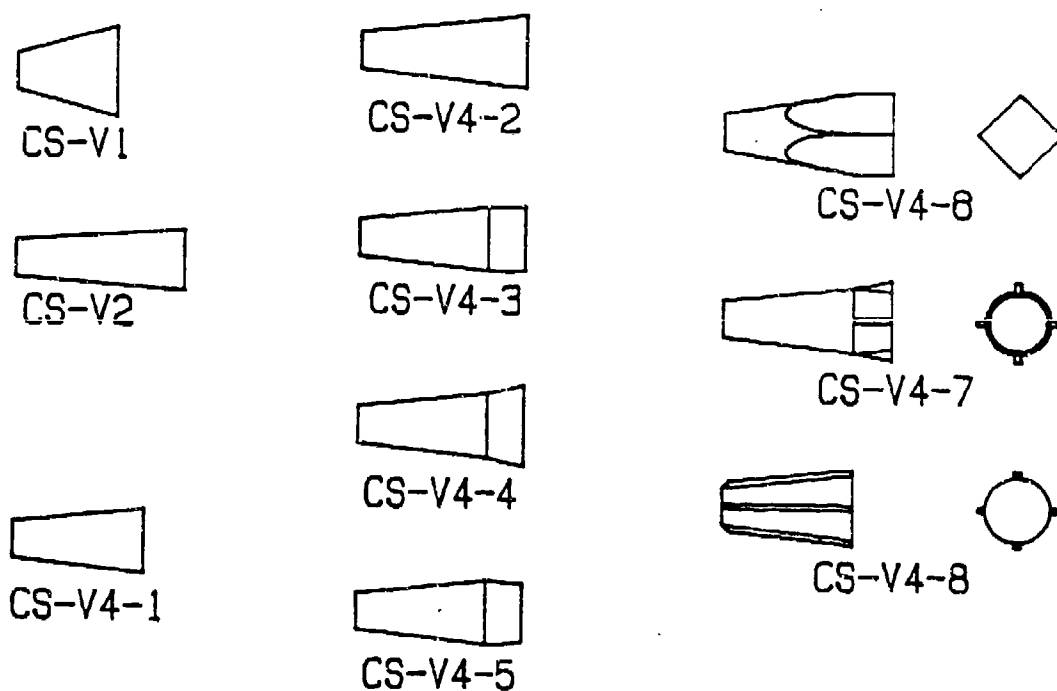


Figure 2. Afterbody and extension configuration.

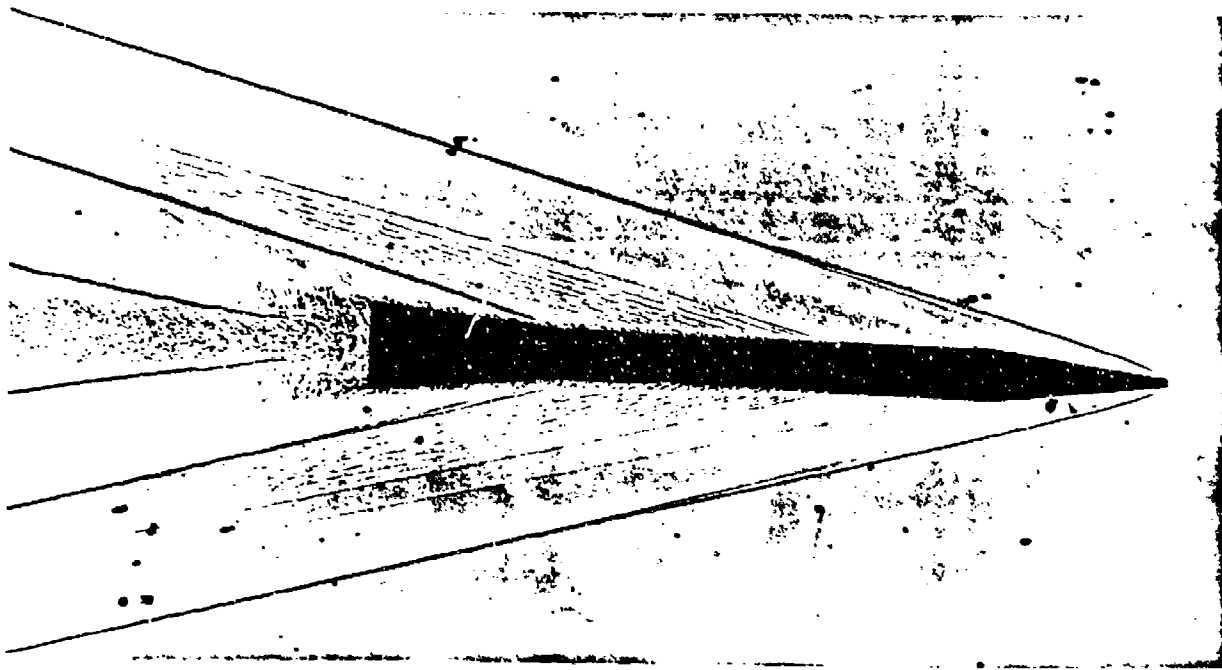


Figure 3. Spark shadowgraph of CS-V4-1 baseline projectile in flight (low yaw).

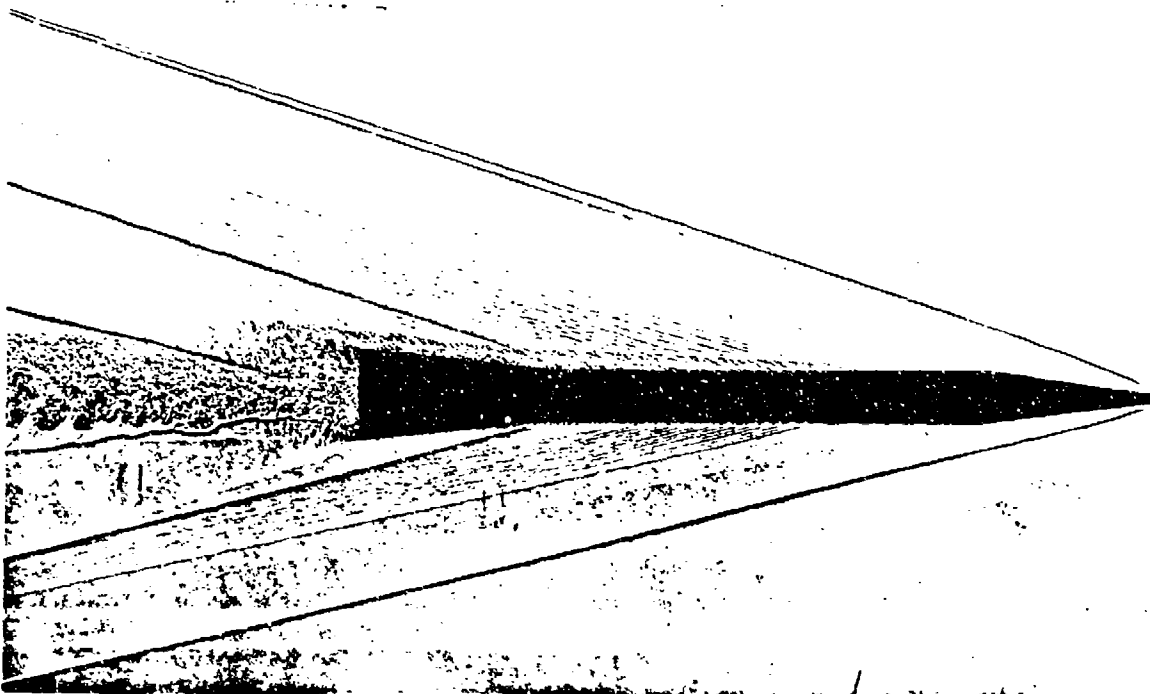


Figure 4. Spark shadowgraph of CS-V4-1 baseline projectile in flight (high yaw).

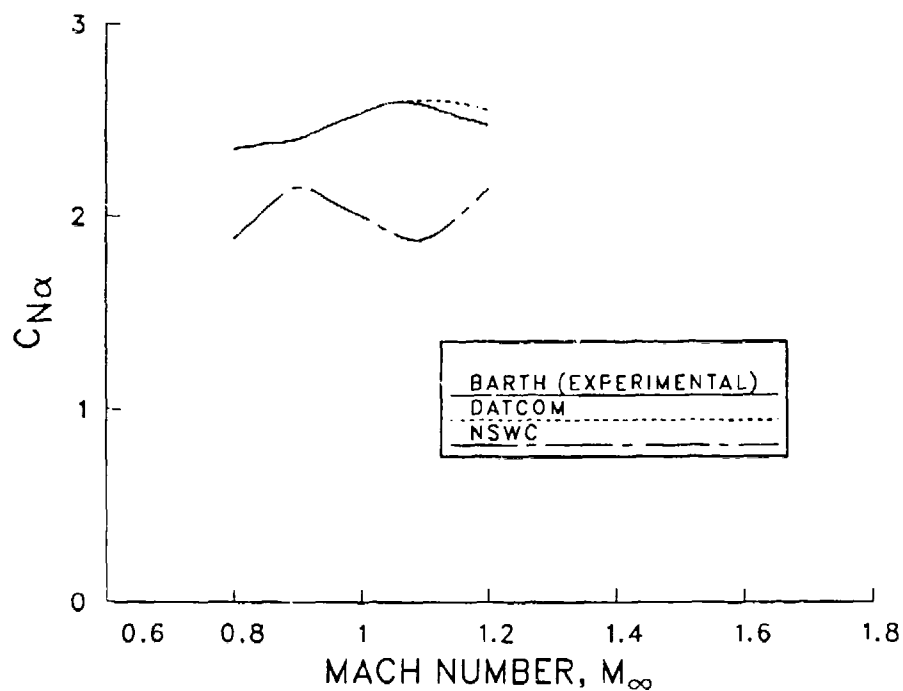


Figure 5. Comparison between predicted characteristics of a cone-cylinder body and Barth's data for the slope of normal-force curve.

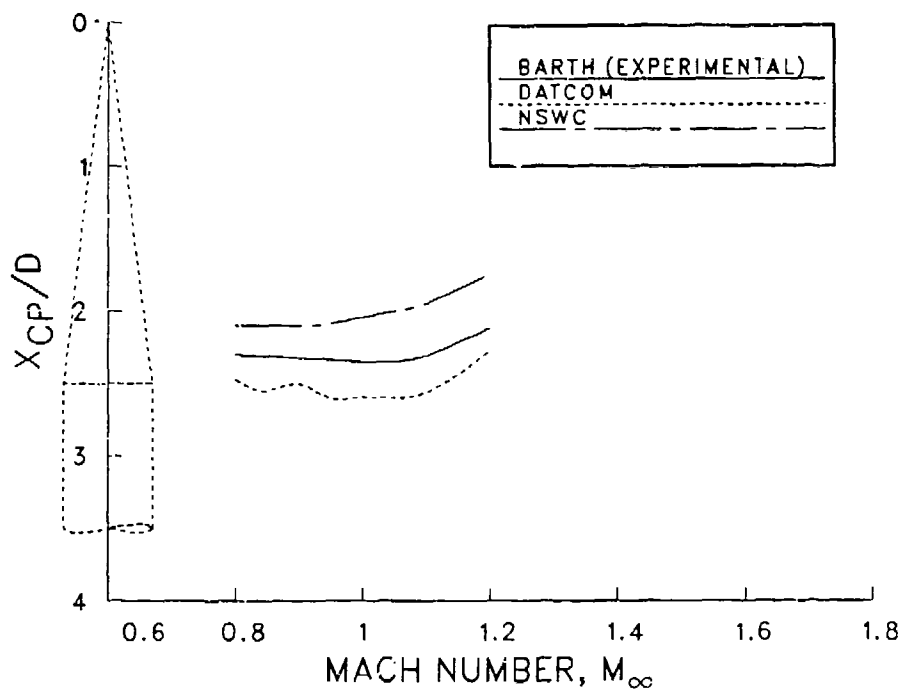


Figure 6. Comparison between predicted characteristics of a cone-cylinder body and Barth's data for the center-of-pressure location.

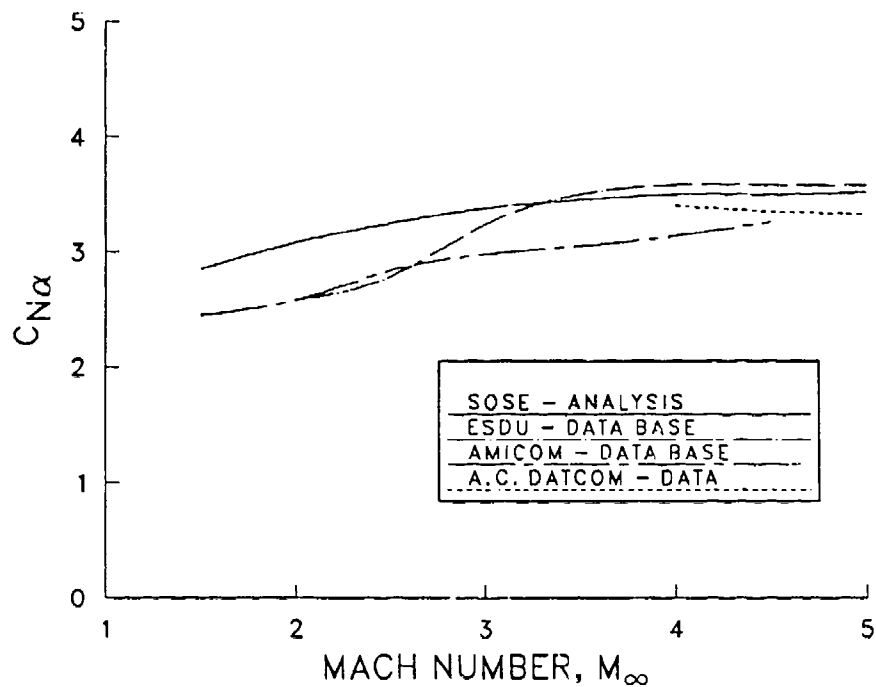


Figure 7. Comparison between computed forebody characteristics for the slope of normal-force curve.

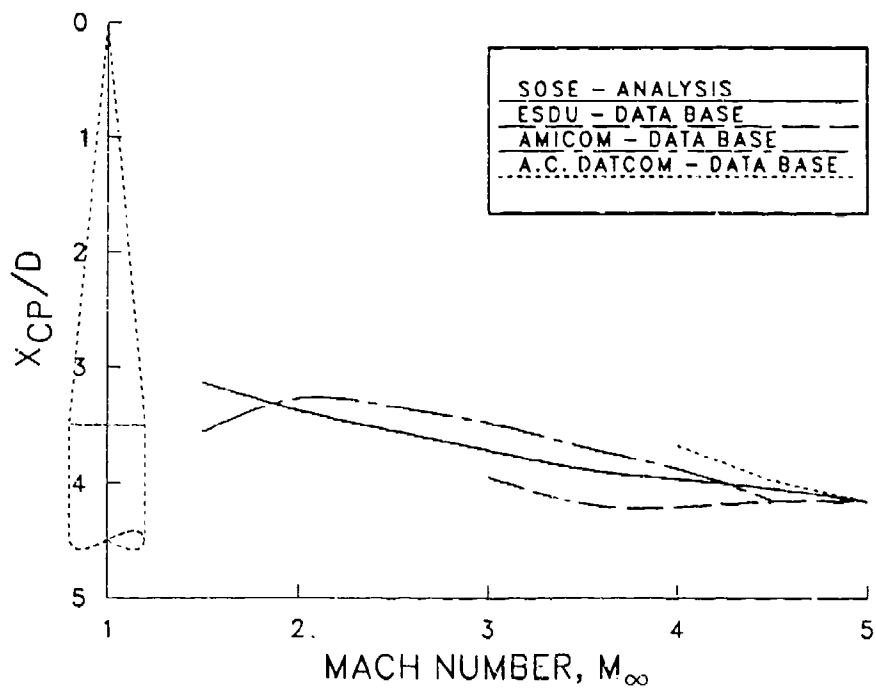
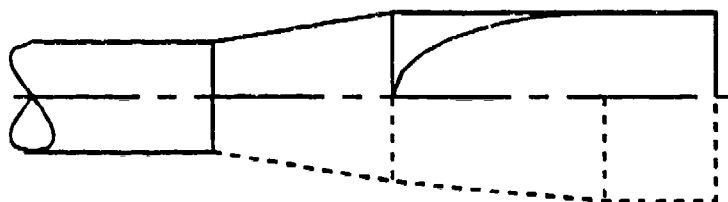
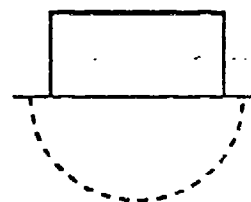


Figure 8. Comparison between computed forebody characteristics and empirical data for the location of center-of-pressure.

CS-V4-6 (Square Base)

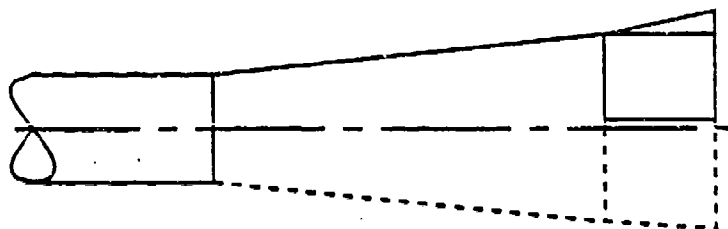


ACTUAL

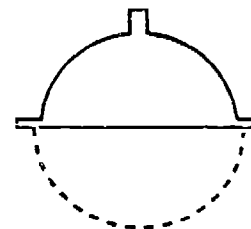


EQUIVALENT

CS-V4-7 (Flare-Fin)

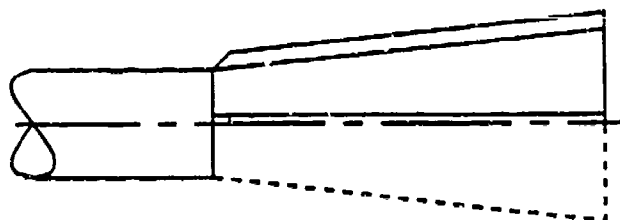


ACTUAL

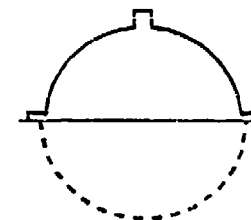


EQUIVALENT

CS-V4-8 (Flare-Strake)



ACTUAL



EQUIVALENT

Figure 9. Geometry of equivalent flare stabilizers.

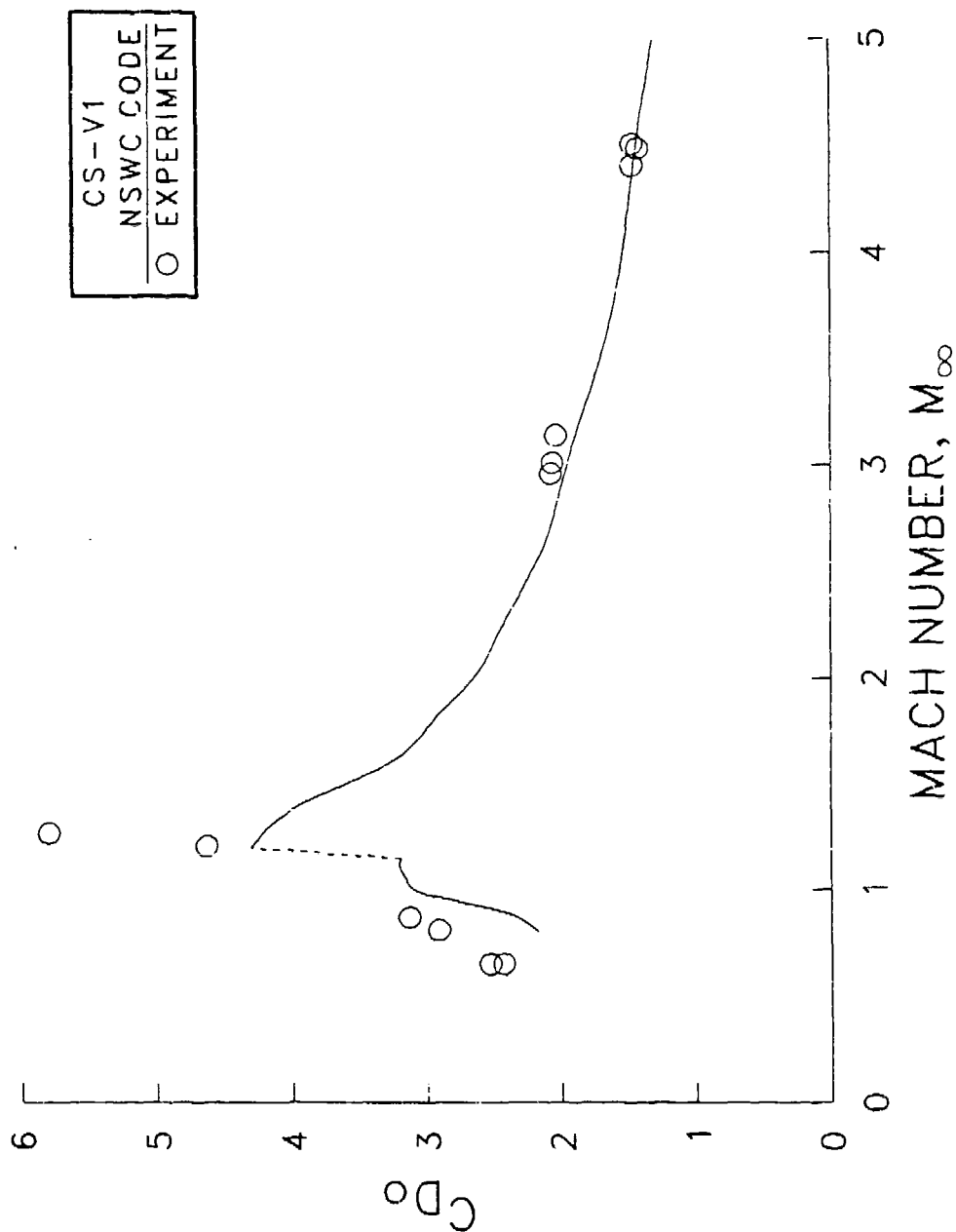


Figure 10. Axial-force coefficient as a function of Mach number
f - the CS-V1 configuration.

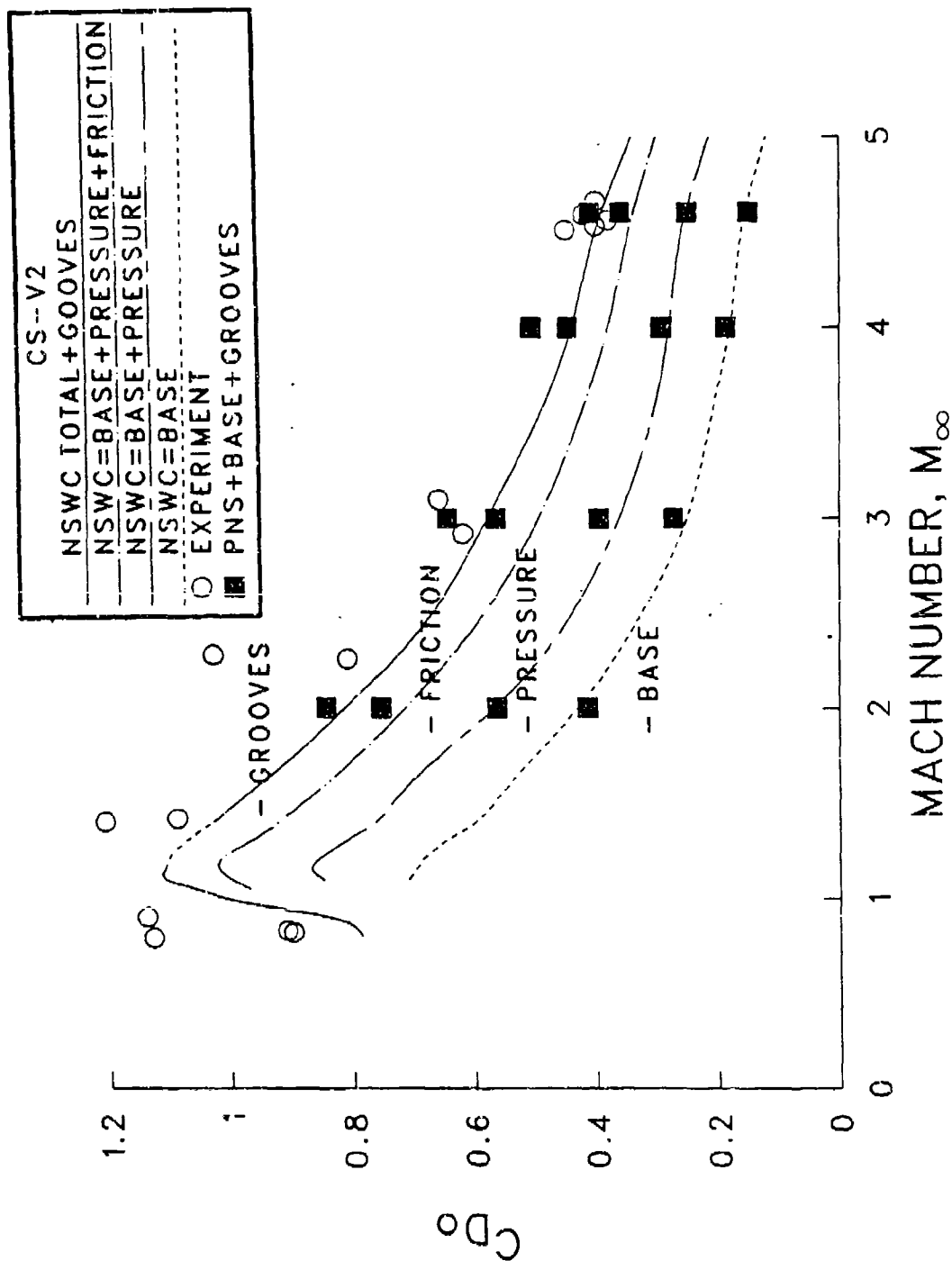


Figure 11. Axial-force coefficient as a function of Mach number with component breakdown for the CS-V2 configuration.

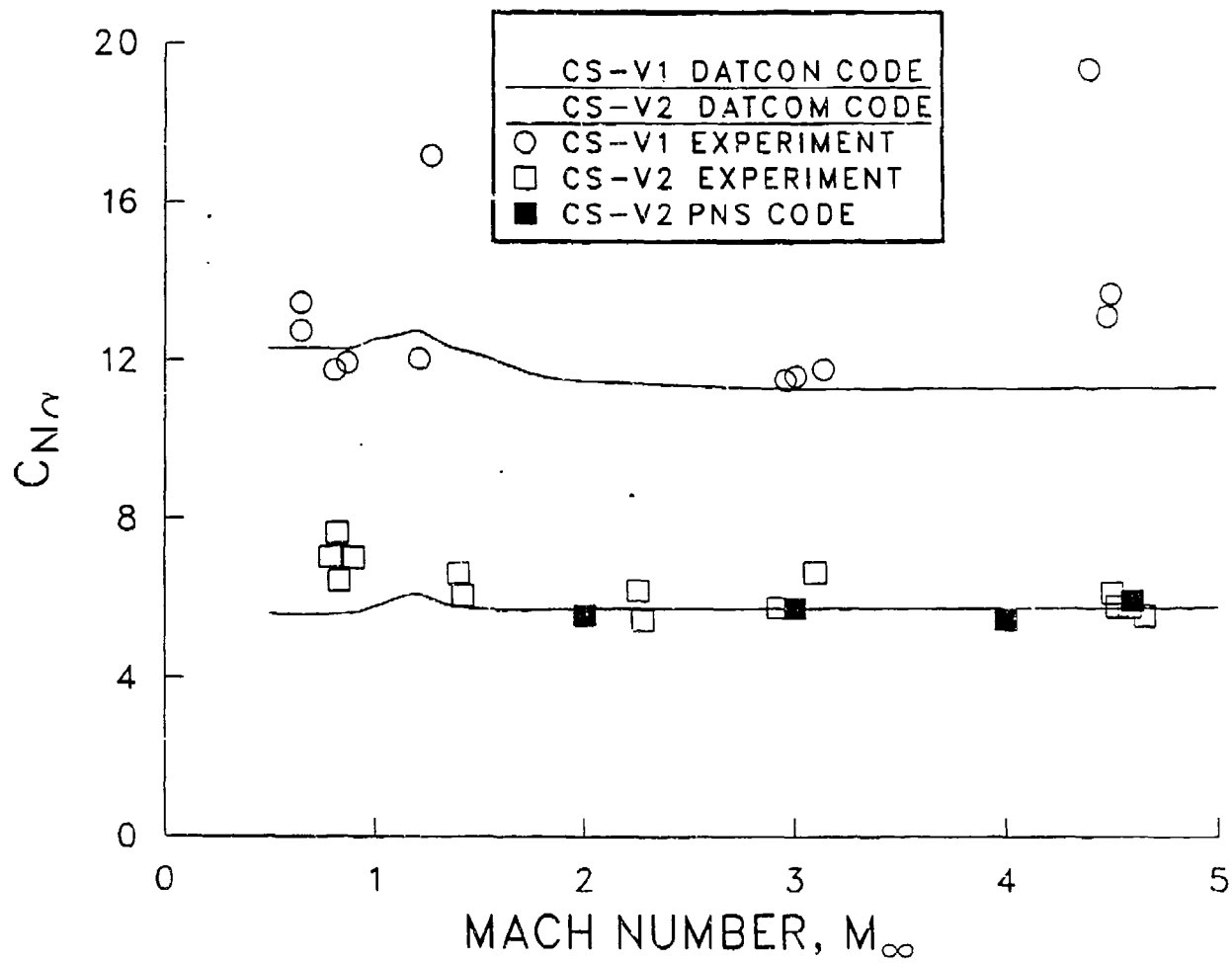


Figure 12. Comparison between analysis and range results for the slope of the normal-force curve as a function of Mach number.

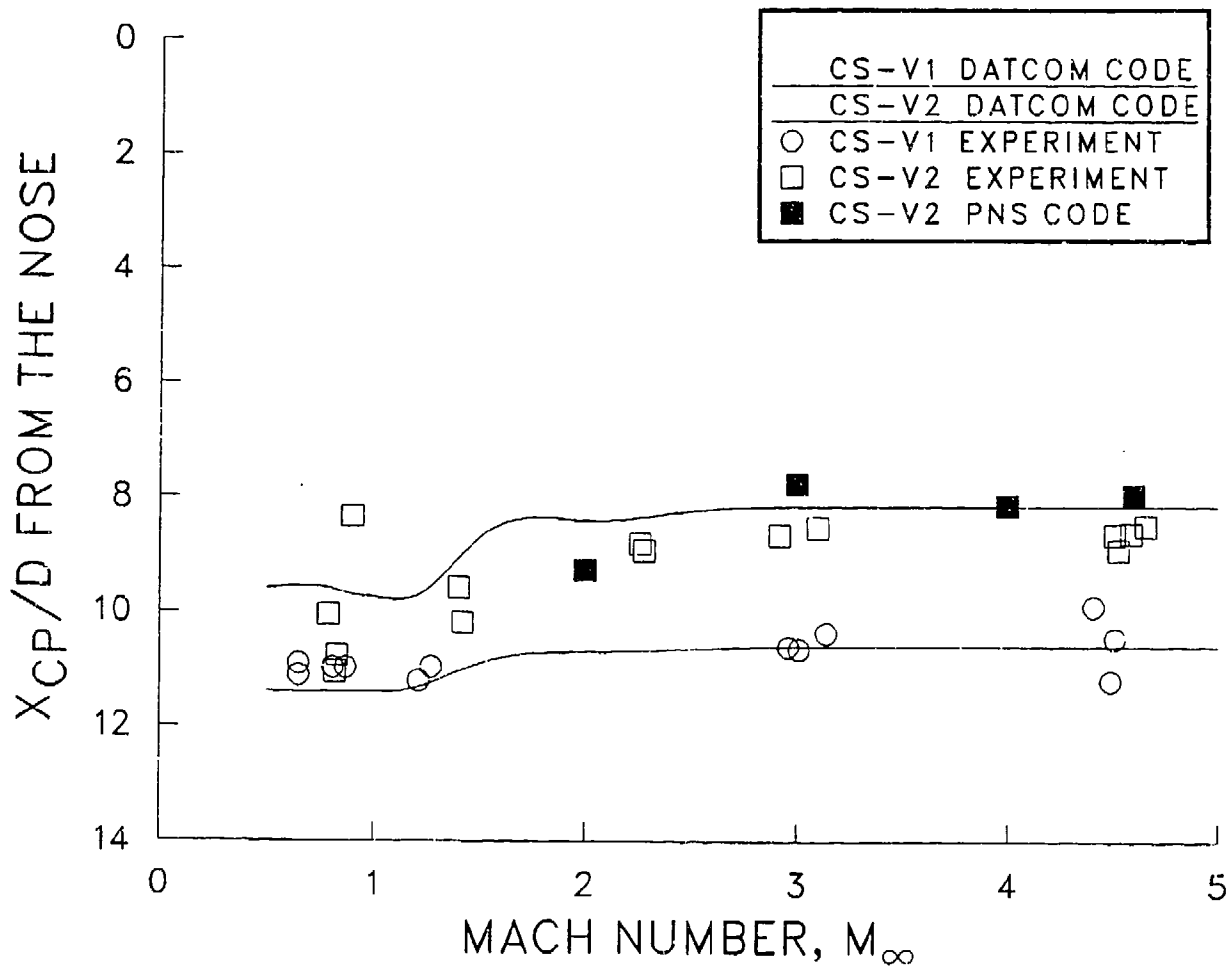


Figure 13. Comparison between analysis and range results for the location of the center-of-pressure as a function of Mach number.

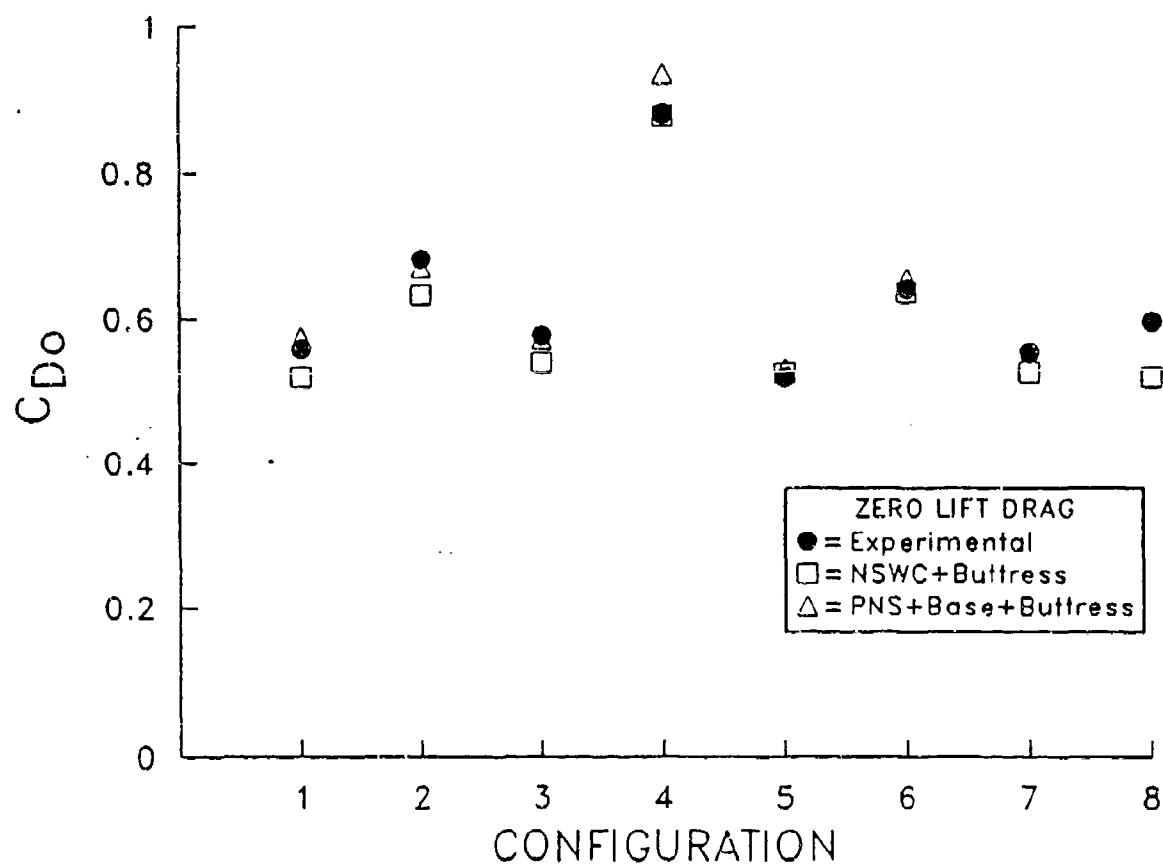


Figure 14. Zero lift drag coefficient for all configurations at $M_\infty=4.0$.

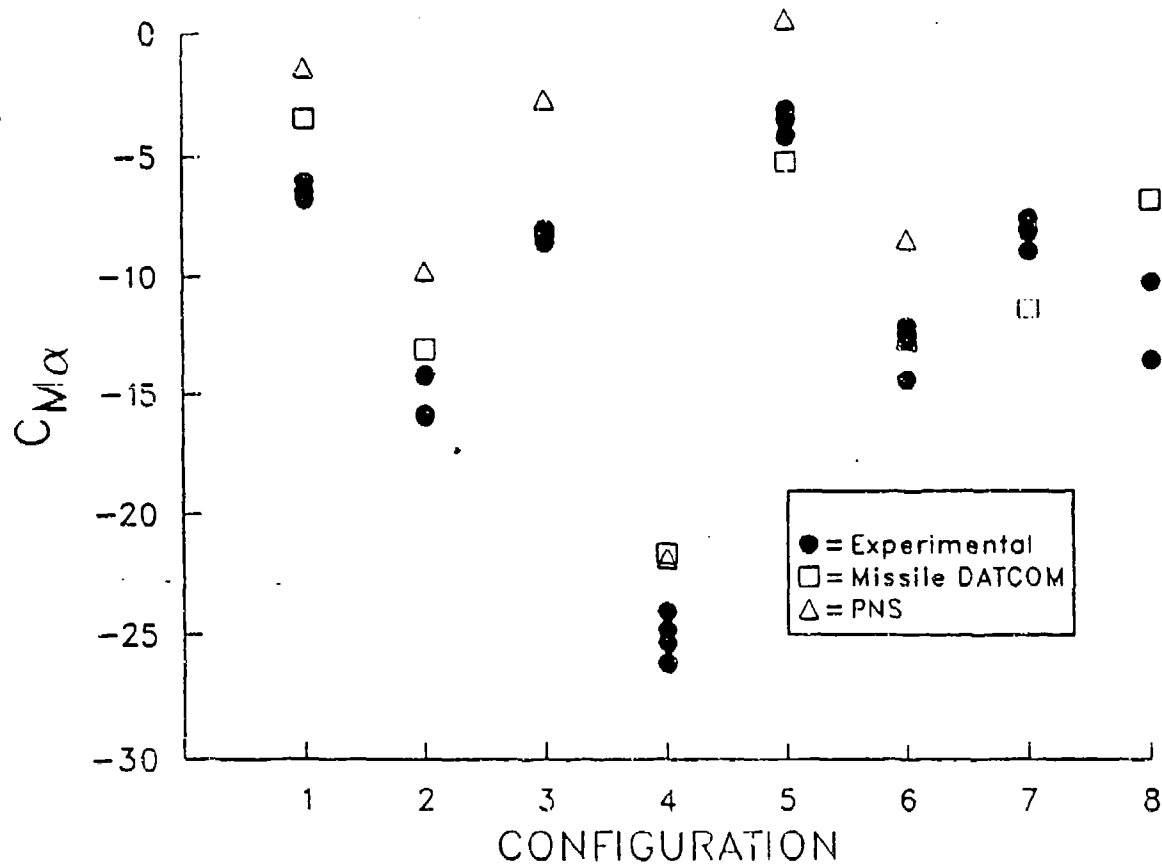


Figure 15. Slope of the pitching moment coefficient about the center of gravity at $M_\infty=4.0$.

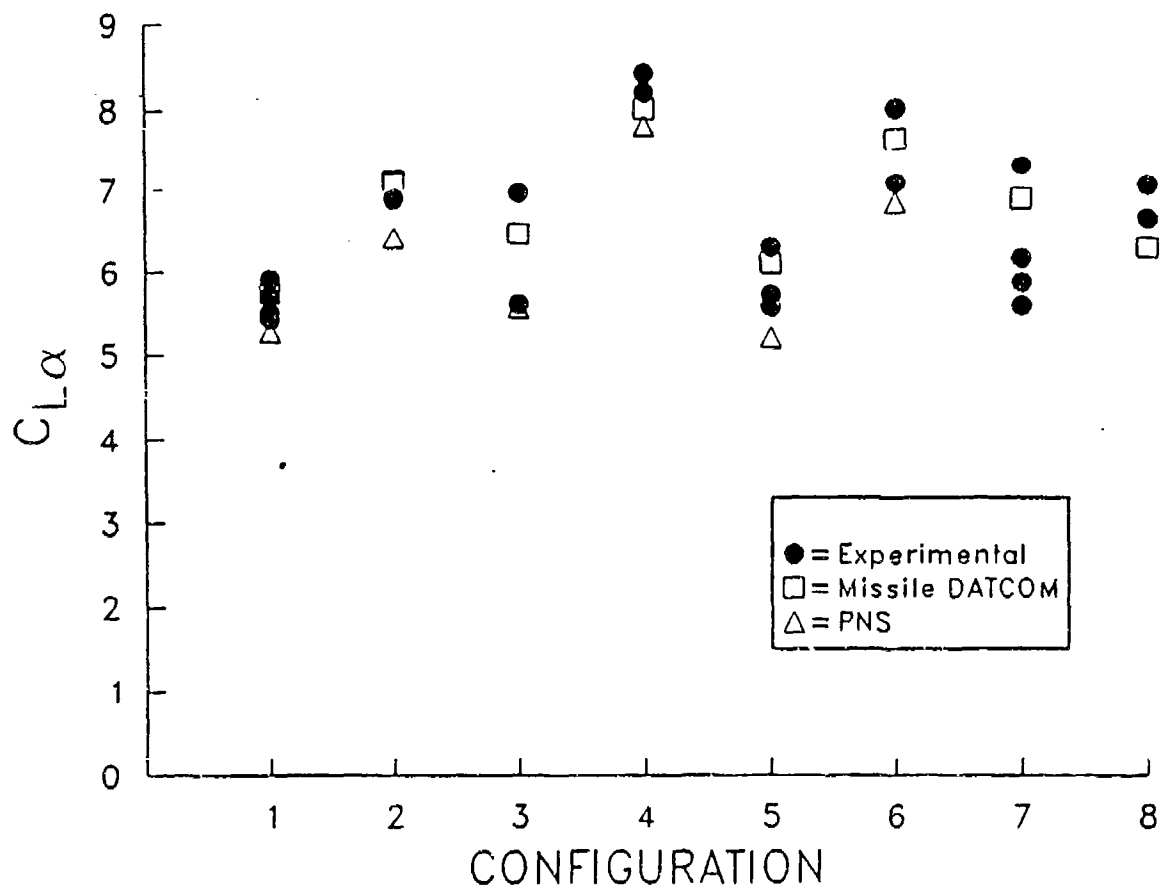


Figure 16. Slope of the lift coefficient for all configurations at $M_\infty=4.0$.

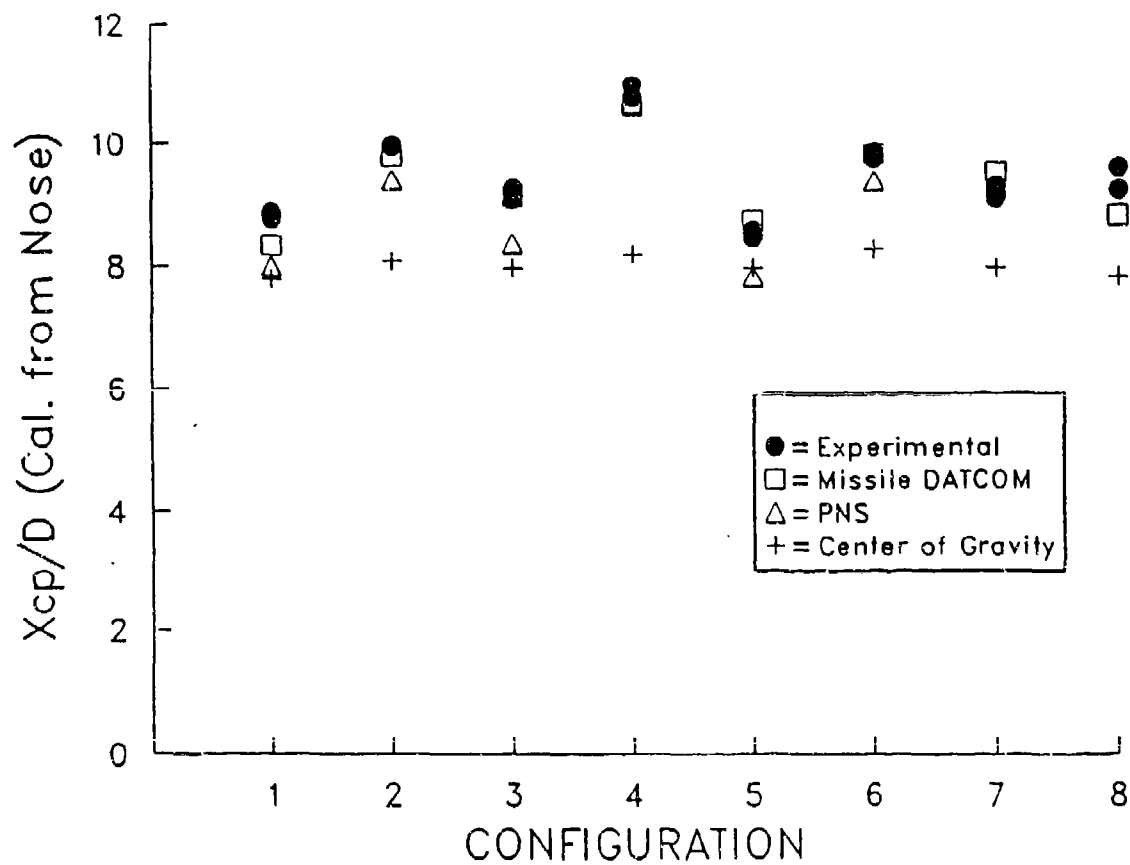


Figure 17. Center of pressure location from the projectile nose for all configurations at $M_{\infty}=4.0$.

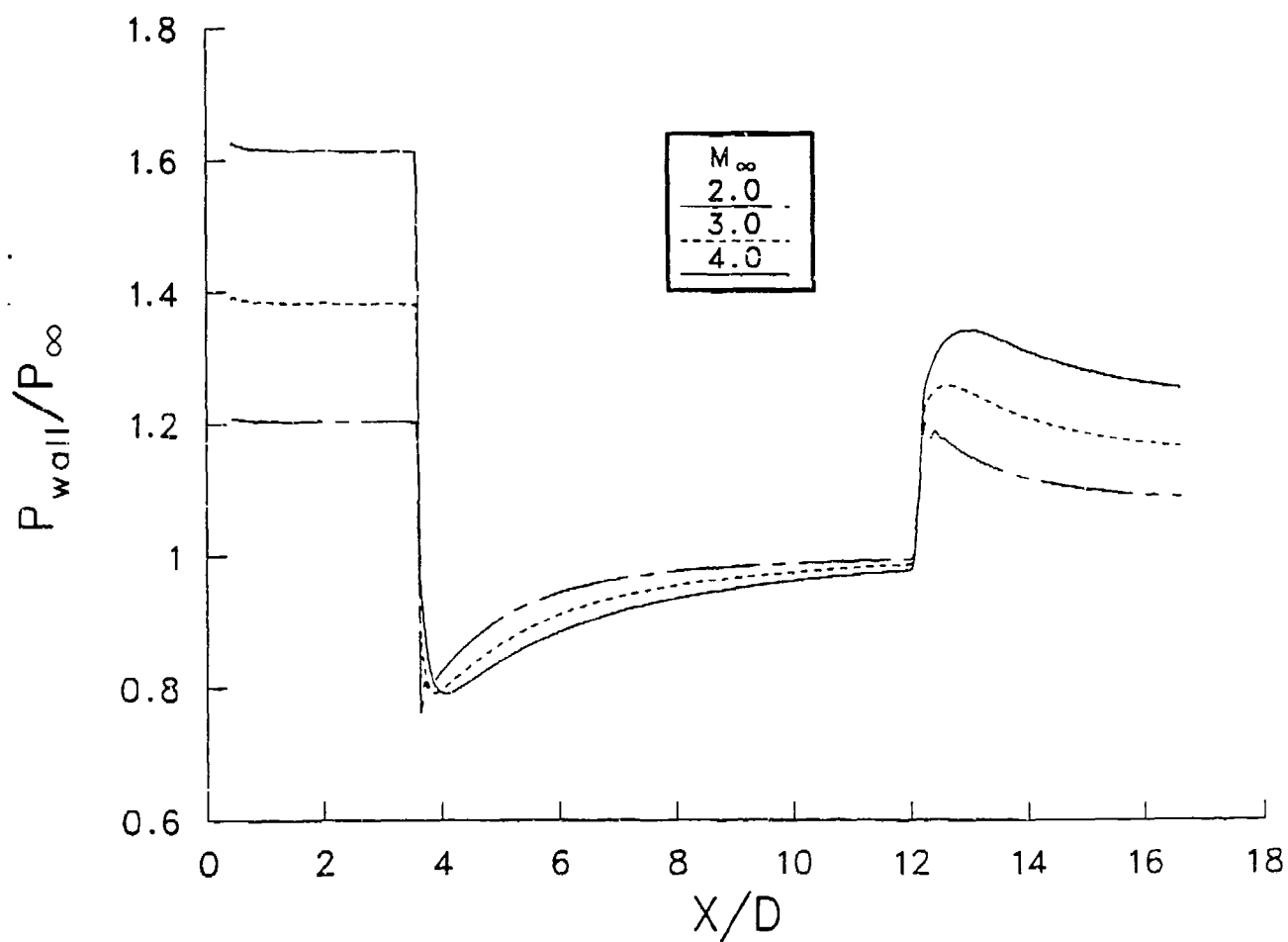


Figure 18. Wall pressure distribution for configuration CS-V2 at three Mach numbers.

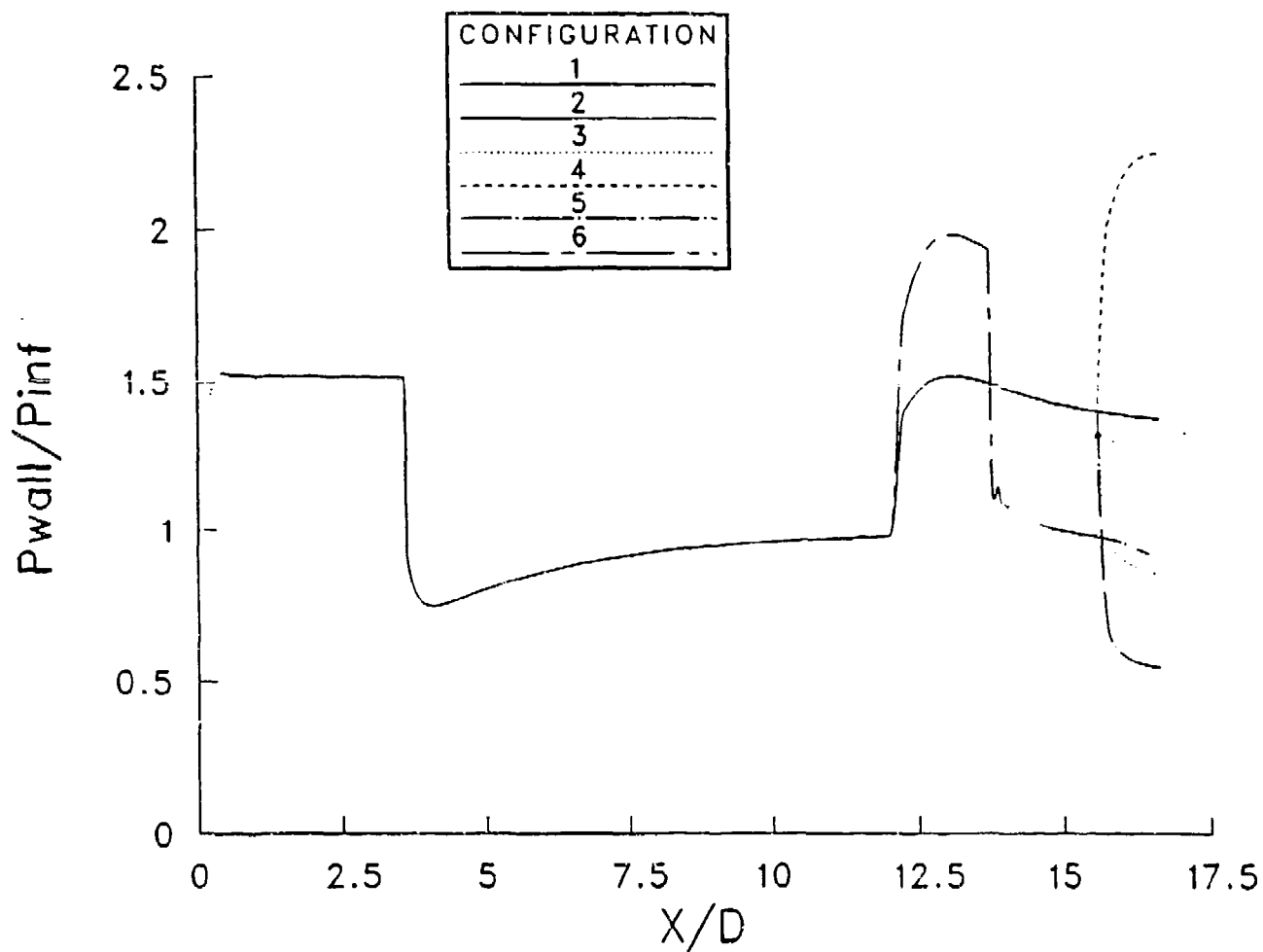


Figure 19. Wall pressure distribution for five configurations $M_{\infty}=4.0$, $\alpha = 1^{\circ}$, leeward.

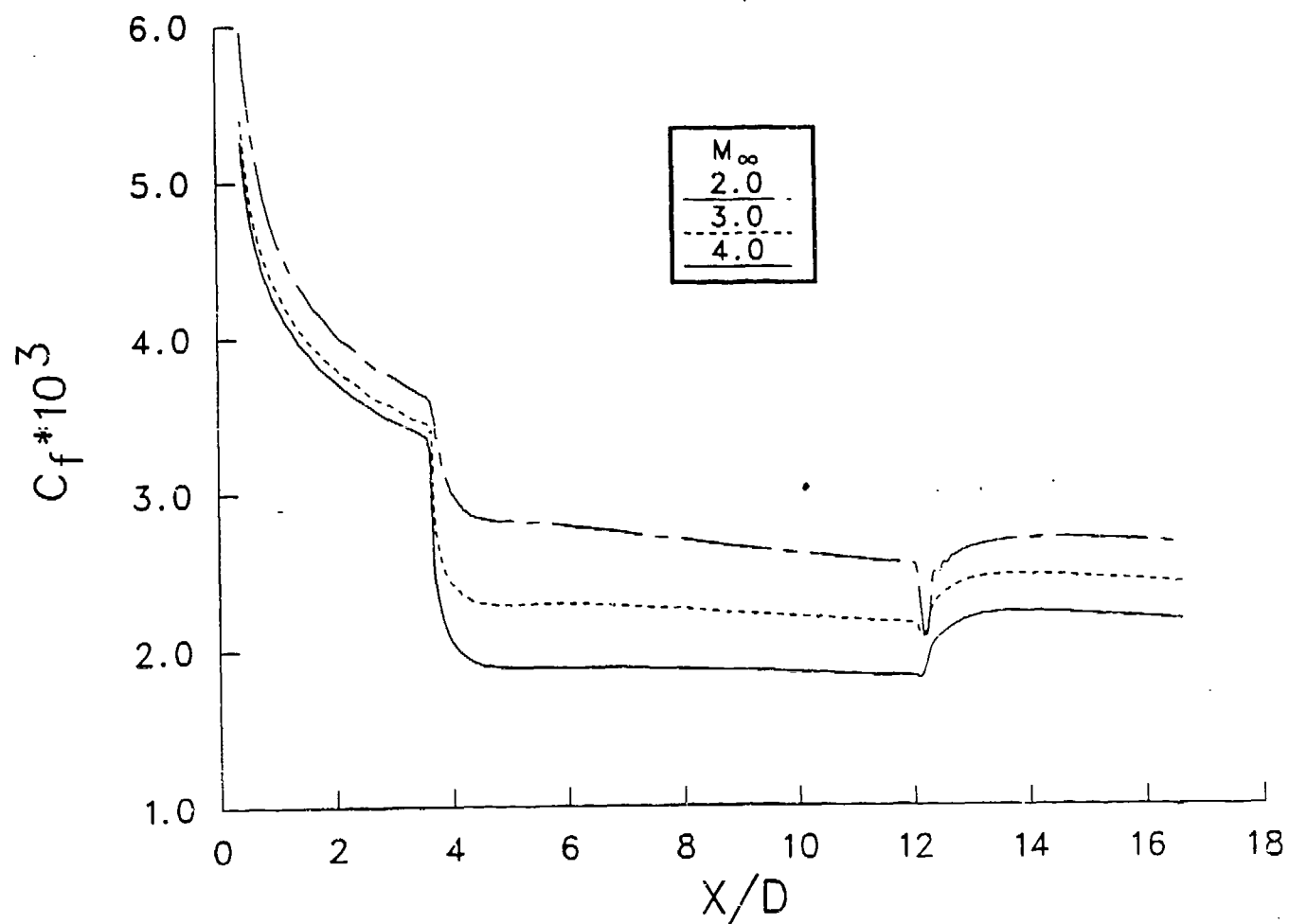


Figure 20. Skin friction coefficient distribution for configuration CS-V2 at three Mach numbers.

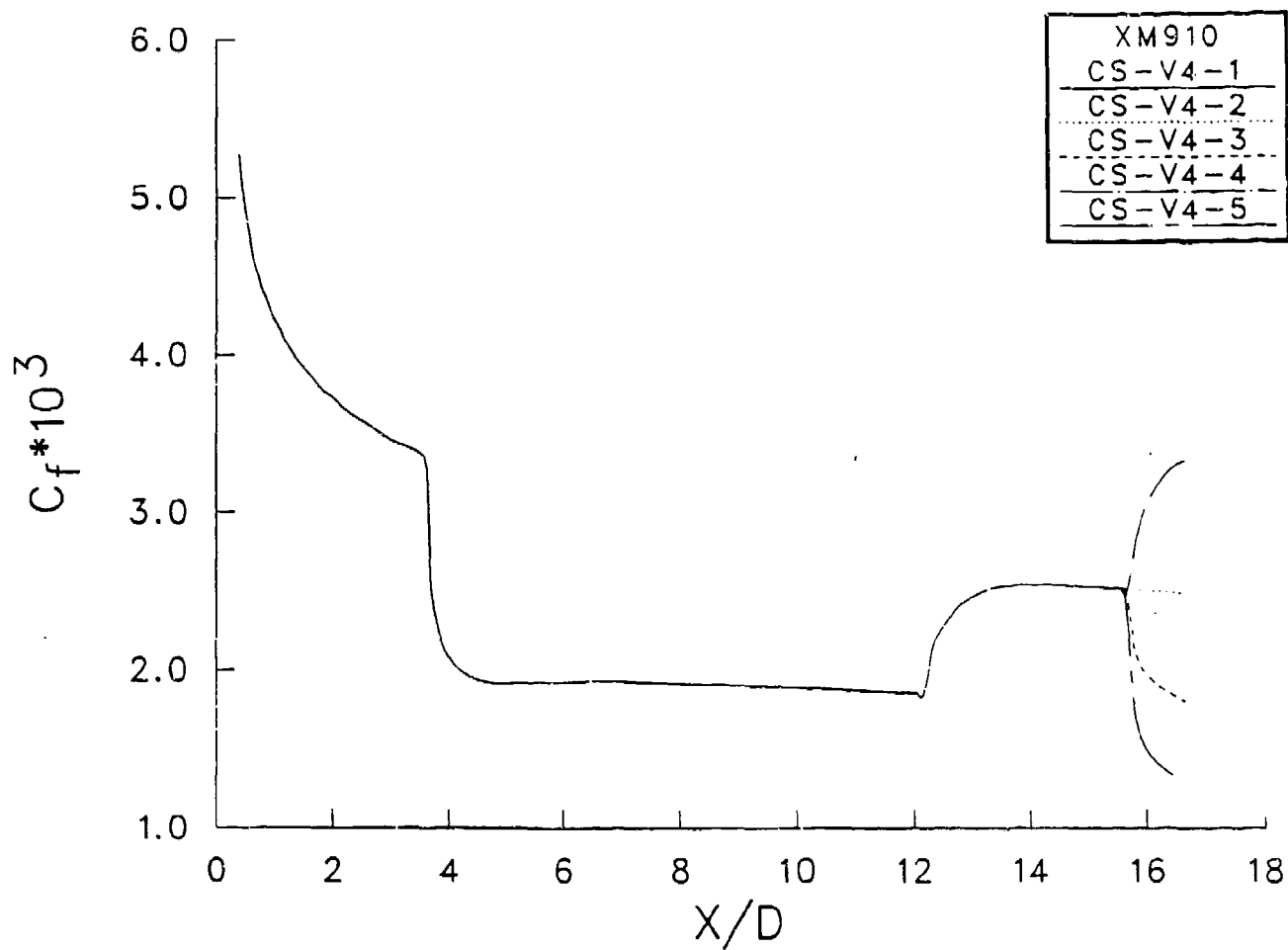


Figure 21. Skin friction coefficient distribution for five configurations at $M_\infty=4.0$, $\alpha=0^\circ$.

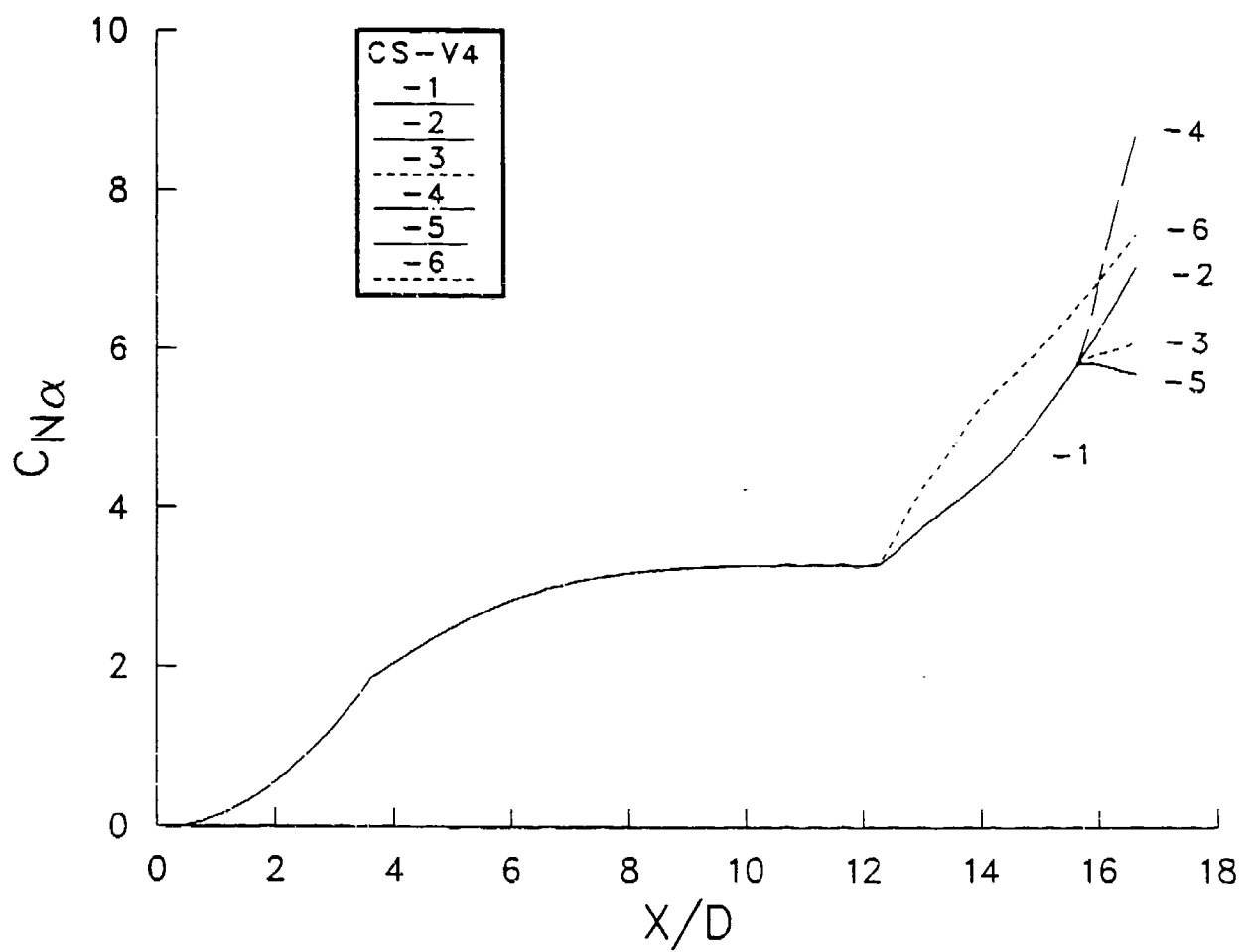


Figure 22. Normal-force distribution for six configurations at $M_\infty=4.0$ $\alpha=0^\circ$.

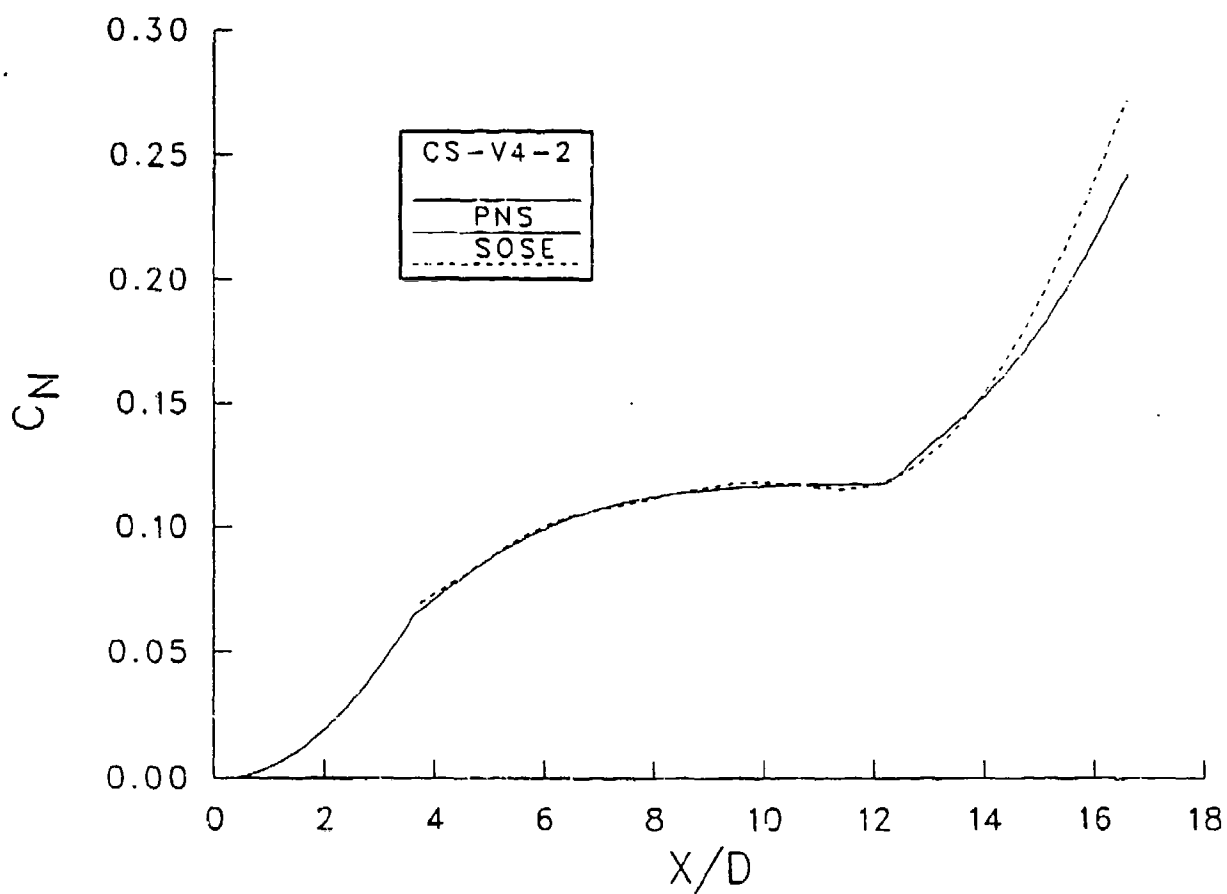


Figure 23. Comparison between Second Order Shock Expansion and PNS normal-force distribution.

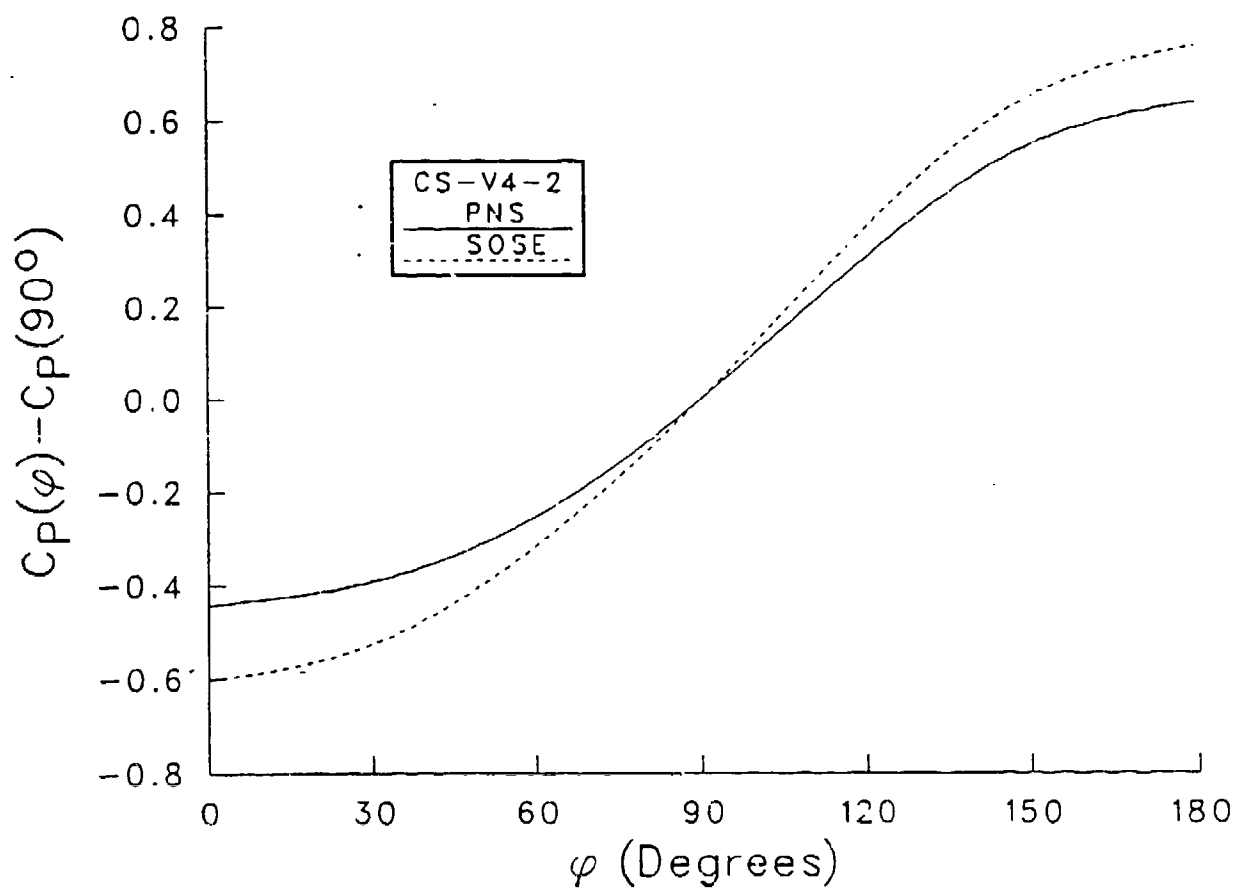


Figure 24. Comparison between Second Order Shock Expansion and PNS circumferential pressure distribution on the flare.

ALL CS-V4 CONFIGURATIONS
M = 4

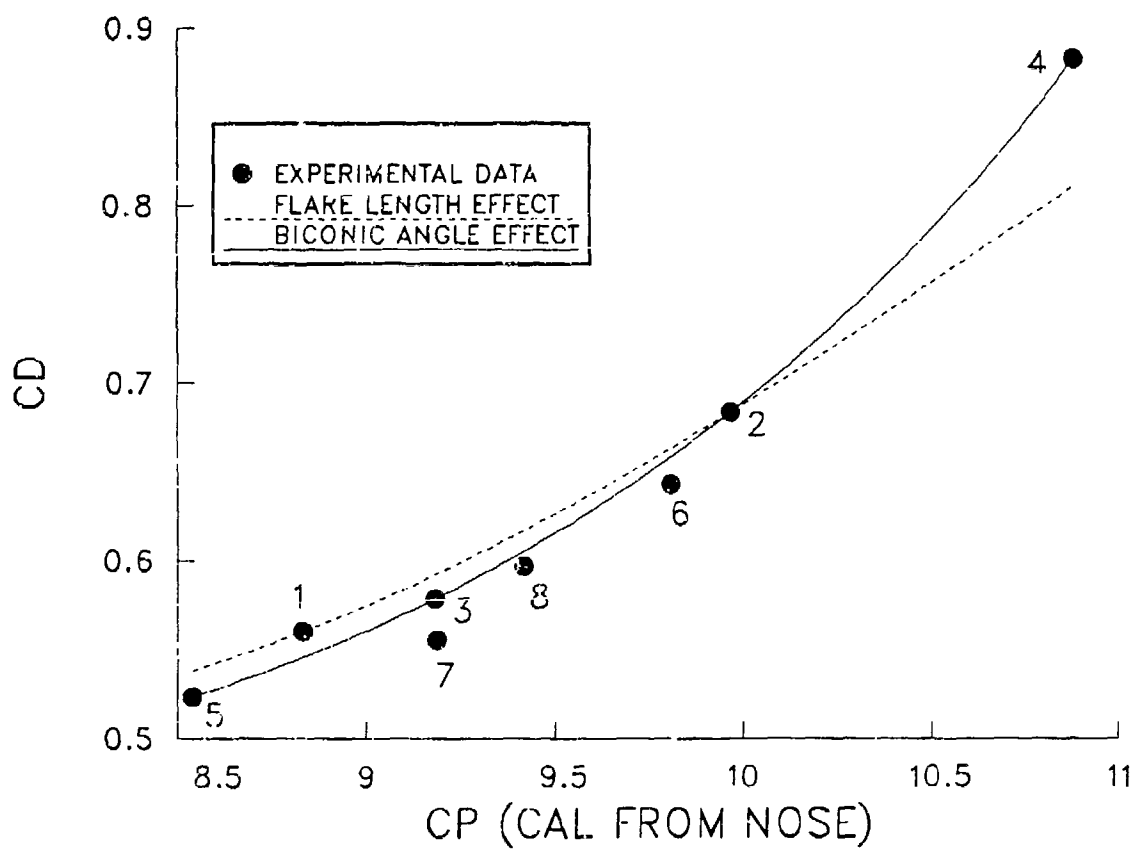


Figure 25. Correlation of drag coefficient with center of pressure location at $M_\infty=4.0$.

REFERENCES

1. I. Celmins, "Aerodynamic Characteristics of Fin- and Flare- Stabilized 25mm Training Round Prototypes," Proceedings 10th International Symposium on Ballistics, Vol. 1, San Diego, California, October, 1987 (also see BRL-TR-2882, U.S. Army Ballistic Research Laboratory, Aberdeen Proving Ground, Maryland, December 1987 (AD A191683)).
2. W.F. Braun, "The Free Flight Aerodynamic Range," BRL Report No. 1048, U.S. Ballistic Research Laboratory, Aberdeen Proving Ground, Maryland, August 1958 (AD 202249).
3. C.H. Murphy, "Data Reduction for the Free Flight Spark Ranges," BRL Report No. 900, U.S. Army Ballistic Research Laboratory, Aberdeen Proving Ground, Maryland, February 1954 (AD 35833).
4. S.R. Vukelich, J.E. Jenkins, "Missile DATCOM: Aerodynamic Prediction of Conventional Missiles Using Component Build- Up Techniques," AIAA Paper No. 84-0388, 1984.
5. L.A. Mason, L. Devan, F.G. Moore, and D. McMillian, "Aerodynamic Design Manual for Tactical Missiles," NSWC TR 81-156 1981.
6. M.D. Van Dyke, "First- and Second-Order Theory of Supersonic Flow Past Bodies of Revolution," Journal of Aerospace Sciences, Vol. 18, No. 3, 1951.
7. C.A. Syvertson, and D.H. Dennis, "A Second-Order Shock Expansion Method Applicable to Bodies of Revolution near Zero-Lift," NACA Report 1328, 1957.
8. H. Barth, "Data for Determining Normal-Force, Moment and Tangential-Force Characteristics of Nose-Cylinder Configurations in the Transonic Velocity Range," MBB Report WE-2-97/69, 1969.
9. A. Sigal, "A Critical Review of Data Bases on the Normal- Force and the Center-of-Pressure Location of Bodies," ARC Report 0-229 (in Hebrew), The Technion, 1985.
10. A. Stoney, "Collection of Zero-Lift Drag Data," NASA TR Report 100, 1962.
11. ESDU Data Units 5.01.03.01 and 5.08.03.01, Engineering and Scientific Data Units International, Ltd., London, Great Britain, 1983.
12. DATCOM-USAF Stability and Control Data Compendium, Second Edition, 1975.
13. D.J. Spring, "The Effect of Nose Shape and Afterbody Length on the Normal Force and Neutral Point Location at Mach Numbers from 0.8 to 4.5," U.S. Army Missile Command, Report No. RF-TR-64-13, 1964.
14. J.N. Nielsen, Missile Aerodynamics, McGraw-Hill Book Company, Inc., New York, New York, 1960.
15. A. Sigal and J.E. Danberg, "Analysis of Turbulent Boundary Layer over Rough Surfaces," U.S. Army Ballistic Research Laboratory, Aberdeen Proving Ground, Maryland, report in progress.

16. R.V. Owens, "Aerodynamic Characteristics of Spherically Blunted Cones at Mach Numbers from 0.5 to 5.0," NASA TN D-3088, 1965.
17. H. Esch, "Bodies," Article No. 4 in "Missile Aerodynamics," AGARD-LS-98, 1979.
18. L.B. Schiff and J.L. Steger, "Numerical Simulation of Steady Supersonic Viscous Flow," AIAA Paper No. 79-0130, 17th Aerospace Sciences Meeting, January 1979.
19. R. Beam and R.F. Warming, "An Implicit Factored Scheme for the Compressible Navier-Stokes Equations," AIAA Journal, Vol. 16, No. 4, pp. 85-129, 1978.
20. T.J. Mueller, C.R. Hail, Jr., and P.J. Roache, "The Influence of Initial Flow Direction on the Turbulent Base Pressure in Supersonic Axisymmetric Flow," AIAA Paper No. 70-555, May 1970.
21. B.S. Baldwin and H. Lomax, "Thin Layer Approximation and Algebraic Model for Separated Turbulent Flows," AIAA Paper No. 78-257, January 1978.

LIST OF SYMBOLS

A	lateral surface area
b	span of the fin or strake
C_D	drag coefficient
C_L	skin friction coefficient
C_p	pressure coefficient
C_L	lift coefficient
C_N	normal-force coefficient
ΔC_N	contribution of flare to normal-force coefficient
C_M	pitching moment coefficient
D	projectile diameter
D_b	base diameter
d	width of a side of a square body
M	Mach number
S	body local cross sectional area
S_{BT}	surface area covered with buttress threads/grooves
S_R	reference area, $\frac{\pi D^2}{4}$
X	distance from projectile nose along the axis of symmetry
X_{CP}	location of the center of pressure

Greek Symbols

α	Angle of attack
η	flare efficiency
ρ	density
ϕ	circumferential angle
ϕ_f	flare angle

Subscripts

b	base
bg	buttress groove
e	equivalent slender body
f	viscous friction
0	zero lift conditions
∞	conditions at infinity

DIS TRIBUTION LIST

<u>No.</u> <u>Copies</u>	<u>Organization</u>	<u>No.</u> <u>Copies</u>	<u>Organization</u>
12	Administrator Defense Technical Information Center ATTN: DTIC-DDA Cameron Station Alexandria, VA 22304-6145	1	Commander US Army Aviation Systems Command ATTN: AMSAV-DACL 4300 Goodfellow Blvd St Louis, MO 63120-1789
1	HQDA (SARD-TR) Washington, DC 20310	1	Director US Army Aviation Research and Technology Activity Moffett Field, CA 94035-1099
1	Commander US Army Material Command ATTN: AMCDRA-ST 5001 Eisenhower Avenue Alexandria, VA 22333-0001		
1	Commander U.S. Army Armament Research, Development & Engineering Center ATTN: SMCAR-MSI Picatinny Arsenal, NJ 07806-5000		
1	Commander U.S. Army Armament Research, Development & Engineering Center ATTN: SMCAR-TDC Picatinny Arsenal, NJ 07806-5000	1	Commander US Army Missile Command ATTN: AMSMI-AS Redstone Arsenal, AL 35898- 5010
1	Commander Benet Weapons Laboratory Armament R&D Center US Army AMCCOM ATTN: SMCAR-LCB-TL Watervliet, NY 12189-4050	1	Commander US Army Laboratory Command ATTN: AMSLC-TD Adelphi, MD 20783-1145
1	Commander US Army Armament, Munitions and Chemical Command ATTN: SMCAR-ESP-L Rock Island, IL 61299-7300		

DISTRIBUTION LIST

<u>No.</u> <u>Copies</u>	<u>Organization</u>	<u>No.</u> <u>Copies</u>	<u>Organization</u>
1	Commander US Army Tank Automotive Command ATTN: AMSTA-DI Warren, MI 48090-5000	5	Director National Aeronautics and Space Administration Ames Research Center ATTN: MS-227-8, L. Schiff MS-258-1, T. Holst MS-258-1, J. Steger MS-258-1, D. Chaussee MS-258-1, M. Rai Moffett Field, CA 94035
1	Director US Army TRADOC Analysis Center ATTN: ATAA-SL White Sands Missile Range, NM 88002-5502		
1	Commandant US Army Infantry School ATTN: ATSH-CD-CSO-OR Fort Benning, GA 31905-5400	5	Commander U.S. Army Armament Research, Development & Engineering Center ATTN: SMCAR-TSS SMCAR-LCA-F J. Grau R. Kline S. Kahn H. Hudgins Picatinny Arsenal, NJ 07806-5000
1	AFWL/SUL Kirtland AFB, NM 87117-6008		
2	Commander Naval Surface Weapons Center ATTN: Code R44 (Dr. F. Priolo) Code R44 (Dr. A. Wardlaw) K-24, Building 402-12 White Oak Laboratory Silver Spring, MD 20903-5000	1	Air Force Armament Laboratory ATTN: AFATL/DLODL Eglin AFB, FL 32542-5438
3	Director National Aeronautics and Space Administration Langley Research Center ATTN: Tech Library Mr. P. J. Bobbitt Mr. D. M. Bushnell Langley Station Hampton, VA 23665		

DISTRIBUTION LIST

<u>No.</u> <u>Copies</u>	<u>Organization</u>	<u>No.</u> <u>Copies</u>	<u>Organization</u>
1	Massachusetts Institute of Technology ATTN: Tech Library 77 Massachusetts Avenue Cambridge, MA 02139	1	University of Illinois at Urbana Champaign Department of Mechanical and Industrial Engineering Urbana, IL 61801
1	Commander US Naval Surface Weapons Center ATTN: Dr. F. Moore Dahlgren, VA 22448	1	University of Maryland Department of Aerospace Engr. ATTN: Dr. J. D. Anderson, Jr. College Park, MD 20742
1	Air Force Armament Laboratory ATTN: AFATL/FXA (Stephen C. Korn) Eglin AFB, FL 32542-5434	1	University of Notre Dame Department of Aeronautical and Mechanical Engineering ATTN: Prof. T. J. Mueller Notre Dame, IN 46556
1	AEDC Calspan Field Service ATTN: MS 600 (Dr. John Benek) AAFS, TN 37389	1	University of Texas Department of Aerospace Engineering and Engineering Mechanics ATTN: Dr. D. S. Dolling Austin, Texas 78712-1055
1	Virginia Polytechnic Institute & State University ATTN: Dr. Clark H. Lewis Department of Aerospace & Ocean Engineering Blacksburg, VA 24061	1	University of Delaware Department of Mechanical Engineering ATTN: Dr. John Meakin Chairman Newark, DE 19716
1	University of California, Davis Department of Mechanical Engineering ATTN: Prof. H.A. Dwyer Davis, CA 95616	1	University of Florida Department of Engineering Sciences College of Engineering ATTN: Prof. C. C. Hsu Gainesville, FL 32611
1	Pennsylvania State University Department of Aerospace Engineering ATTN: Dr. G. S. Dulikravich University Park, PA 16802		

DISTRIBUTION LIST

<u>No.</u> <u>Copies</u>	<u>Organization</u>	<u>No.</u> <u>Copies</u>	<u>Organization</u>
2	USAF Wright Aeronautical Laboratories ATTN: AFWAL/FIMG Mr. Norman E. Scaggs Dr. J. Shang WPAFB, OH 45433-6553	1	United Technologies Corporation Chemical Systems Division ATTN: Mr. A. L. Holzman P.O. Box 50015 600 Metcalf Road San Jose, CA 95150-0015
1	Grumman Aerospace Corporaton Aerophysics Research Department ATTN: Dr. R. E. Melnik Bethpage, NY 11714	1	Ford Aerospace and Communications Corporation Aeronutronics Division ATTN: Charles White Bud Blair Ford Road Newpoint Beach, CA 92658
1	Advanced Technology Center Arvin/Calspan Aerodynamics Research Department ATTN: Dr. M. S. Holden P. O. Box 400 Buffalo, NY 14225	1	Honeywell Inc. ATTN: Wilford E. Martwick Ken Sundeen 600 Second Street, North East Hopkins, MN 55343
2	Director Sandia National Laboratories ATTN: Dr. W. Oberkampf Dr. F. Blottner Division 1636 Albuquerque, NM 87185		Aberdeen Proving Ground
1	The University of Arizona Aerospace Engineering Department ATTN: Prof. I. Wygnanski Tucson, AZ 85721		Director, USAMSAA ATTN: AMXSY-D AMXSY-MP, H. Cohen
1	Applied Technology Associates ATTN: Mr. R. J. Cavalleri P.O. Box 19434 Orlando, FL 32814		Commander, USATECOM ATTN: AMSTE-TO-F Cdr, CRDC, AMCCOM ATTN: SMCCR-MU SMCCR-RSP-A SMCCR-SPS-IL

USER EVALUATION SHEET/CHANGE OF ADDRESS

This laboratory undertakes a continuing effort to improve the quality of the reports it publishes. Your comments/answers below will aid us in our efforts.

1. Does this report satisfy a need? (Comment on purpose, related project, or other area of interest for which the report will be used.) _____

2. How, specifically, is the report being used? (Information source, design data, procedure, source of ideas, etc.) _____

3. Has the information in this report led to any quantitative savings as far as man-hours or dollars saved, operating costs avoided, or efficiencies achieved, etc? If so, please elaborate. _____

4. General Comments. What do you think should be changed to improve future reports? (Indicate changes to organization, technical content, format, etc.) _____

BRL Report Number _____ Division Symbol _____

Check here if desire to be removed from distribution list. _____

Check here for address change. _____

Current address: Organization _____
Address _____

-----FOLD AND TAPE CLOSED-----

Director
U.S. Army Ballistic Research Laboratory
ATTN: SLCBR-DD-T(NEI)
Aberdeen Proving Ground, MD 21005-5066

OFFICIAL BUSINESS
PENALTY FOR PRIVATE USE \$300



NO POSTAGE
NECESSARY
IF MAILED
IN THE
UNITED STATES

Director
U.S. Army Ballistic Research Laboratory
ATTN: SLCBR-DD-T(NEI)
Aberdeen Proving Ground, MD 21005-9989